

# Week 1

## 1.1 What is ISIS?

ISIS is a research facility at the Rutherford Appleton Laboratory which uses neutrons and muons to study materials at an atomic level, sustaining further research in various other fields. The basics of these studies lie in neutron scattering, a technique which allows for a highly detailed image of the crystal lattice structure of matter and how it behaves in various conditions.

The ISIS accelerator produces the high-energy beams required to penetrate into the materials. It takes hydrogen ions, accelerates them and strips off the electrons leaving a beam of protons. These protons are further accelerated to 800 MeV and focused onto a tungsten target, producing neutron pulses. Finally, the neutrons are detected after interacting with a material.

The neutrons are collected by about 20 instruments, each designed for a specific type of experiment: neutron spectroscopy, diffraction, reflectometry or small angle scattering. In these instruments, various detectors register the position and time of arrival of the impinging neutrons.

Muons are also produced at ISIS from 2-3% of the proton beam by inserting a carbon target, resulting in pions which decay into muons. They may provide complementary information to that attained in neutron experiments because they have a spin and interact with the magnetic properties of the material. The nuclear spin rotates the spin of the muons, making them useful in studying superconducting samples, semiconductors and chemical reactions.

The data from ISIS is used in areas such as energy, nanotechnology, materials processing, drug design, bio-technology. The effect of strains and stresses is investigated in engineering components; analyses are made on the compatibility of bio-materials, the structure of pharmaceutical compounds, or the efficiency of enzymes in removing environmental contamination.

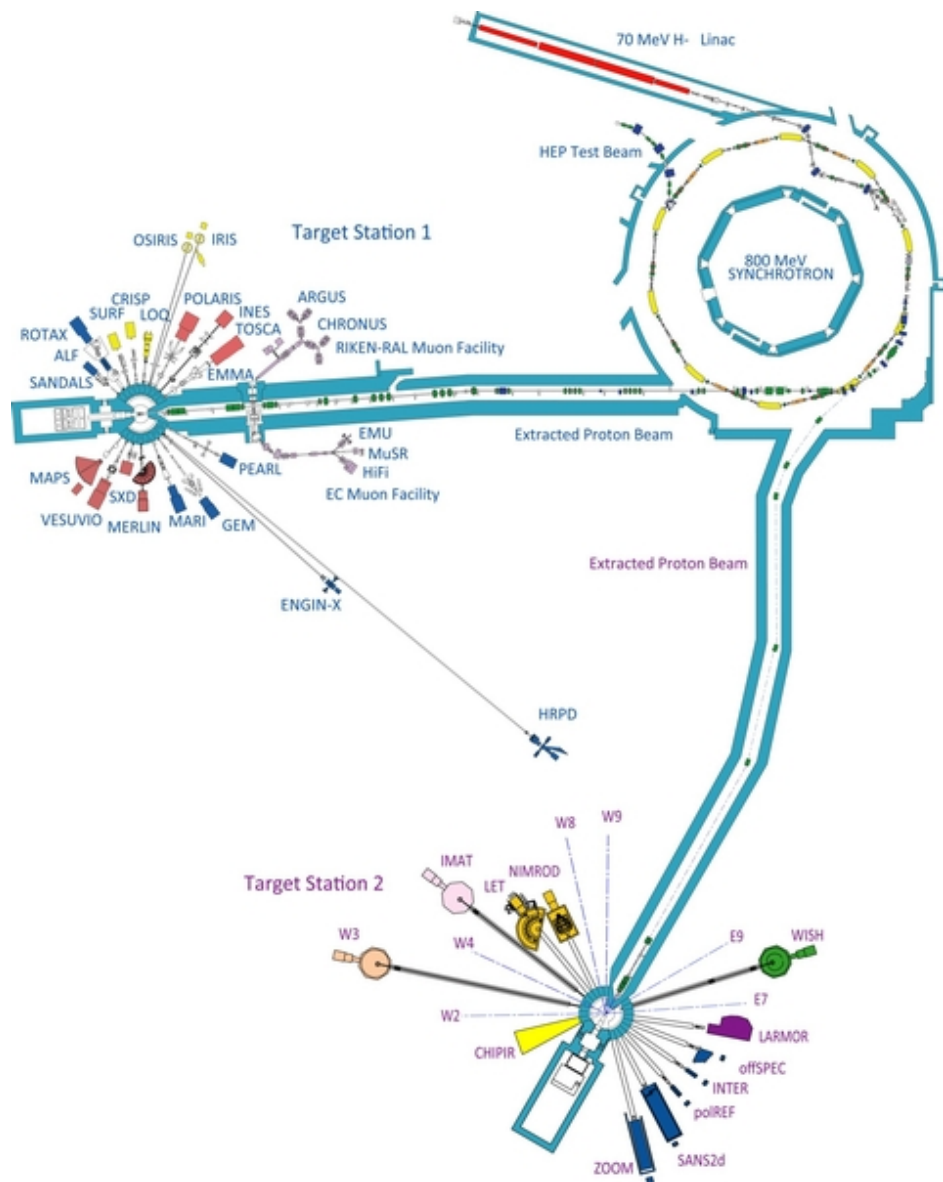


Figure 1.1: ISIS Facility

---

ISIS Instruments, Credit: STFC, <http://www.stfc.ac.uk/stfc/cache/file/24C09892-BF82-4C27-80C9B5567C033C82.jpt>

## 1.2 The ISIS accelerator

The principal components of ISIS are: the Linac, the Synchrotron, Target Station 1, Target Station 2 and the Muon Target. The beam starts as  $200 \mu\text{s}$  pulses passed into the linac, where the RFQ (Radio Frequency Quadrupole, 202.5 MHz) divides the particles in discrete 4.94 ns bunches. The linac provides  $200 \mu\text{s}$  long ,  $22 \text{ mA}$  H- pulses to the synchrotron. At the exit of the synchrotron, two 100 ns long pulses consisting of  $4 \mu\text{C}$  of protons are delivered to the targets. By repeating the entire accelerating process 50 times per second, the final beam current is  $200 \mu\text{A}$ .

### The Linac

As a first element of the linac, the ion source produces H- ions. This is done by feeding the ion source with hydrogen gas and caesium vapour. Positively charged ions are attracted from the formed discharge plasma towards a cathode. Caesium is used because its deposition reduces the work function of the cathode, making it a more efficient donor of electrons to the positively charged hydrogen ions, thus enhancing the production of H-. The extracted beam is passed through a  $90^\circ$  magnet to remove any electrons, and it is accelerated through a DC gap between the high voltage platform (containing the ion source) and the RFQ. There is an additional focusing and monitoring process in the Low Energy Beam Transport before the RFQ.

In the next element, the RFQ, quadrupole electrodes produce a gradient field which both focuses and accelerates the beam. The particles pass through four tanks which are fed with RF fields. Inside each tank, the beam is in step with the alternating field, being shielded inside drift tubes while the field is in the decelerating direction and crossing the gaps between the tubes while the field is in the accelerating direction.

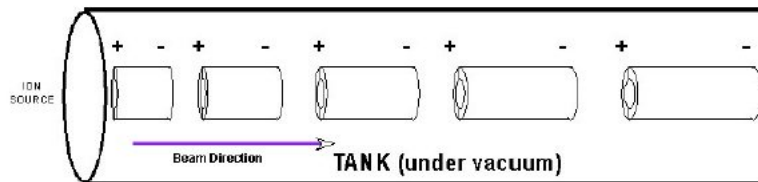


Figure 1.2: One tank from the LINAC

The linac is needed because it accelerates the particles to an injection kinetic energy which reduces the total time needed to obtain the output

energy by accelerating the particles in the ring. Low energy protons have a higher time of flight around the ring, so it is an advantage to have a higher value of the starting injection energy.

### The ISIS synchrotron

In a synchrotron the field is increased with the change in momentum of the particle such that the radius of the orbit remains the same while the particle is accelerated and hence the particle is kept inside the accelerator.

The ISIS synchrotron is a 26 m radius ring in which the protons revolve around 10 thousand times. The major components are the RF cavities used for acceleration, the dipole magnets for bending the beam and quadrupole/sextupole magnets to keep the beam focused.

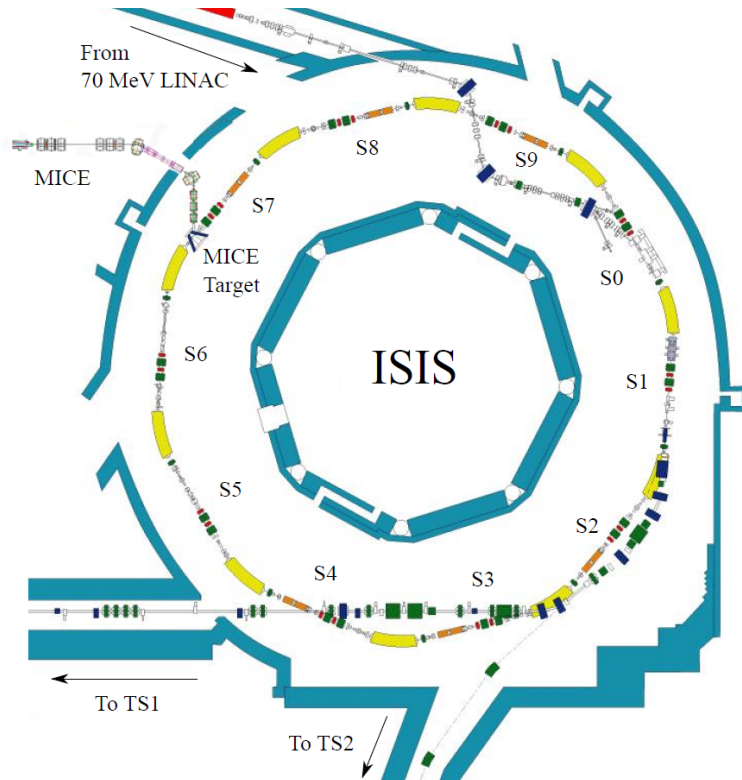


Figure 1.3: ISIS synchrotron (Credit: STFC)

The beam enters from the linac in pulses by the accumulation of a large number of protons over approximately 130 revolutions. The beam is accumulated by a process called “charge exchange injection”: the injected beam and the one already in the ring hit an aluminium oxide foil. This strips off

the electrons from the protons allowing the circumvention of Liouville's theorem, which states that it is impossible to increase the density of particles in phase space by means of conservative forces.

Once injection is complete, the RF system traps the beam into two bunches. There are six double-gap, ferrite-tuned RF cavities which provide the accelerating voltage synchronised with the changing magnetic field in the dipoles. To get the beam out, a system of fast ( $100\text{ ns}$ ) kicker magnets is turned on.

The main advantage of the synchrotron consists in the high energy of the beam that is produced with less hardware compared to that required by a lina. The high energy makes measurements possible in real time.

### Dealing with electrons

When dealing with electron machines, the synchrotron radiation loss has to be taken into consideration (energy loss ratio is  $10^{13}$  compared to protons of the same momentum in the relativistic region). The electrons, being much lighter than the protons, suffer from considerable radiation loss in energy and this may be handled by either using linear accelerators or circular one with large radii. Because of this loss, the accelerating process requires a longer time and more power. The maximum beam energy is given by the point at which the amount of energy loss by radiation is close to the amount of energy added each cycle. Nevertheless, the synchrotron radiation can be useful in producing synchrotron light (X-rays) for probing deep into the structure of matter.

## 1.3 From cyclotrons to FFAG

The cyclotron was one of the first types of circular accelerators. It uses a static magnetic field and an alternating electric field. It is made from two “D”-shaped metal halves insulated from each other and placed into vacuum, connected to an oscillating potential. Below and above the vacuum chamber, there are two magnets (usually magnetic coils) which create a constant field across the chamber, perpendicular to the electrodes plane.

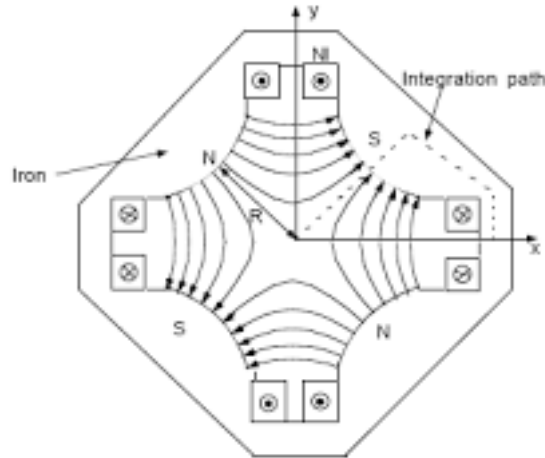
Particles are injected at the centre and because of their increasing momentum, they follow a spiral path being accelerated each time they pass through the gap between the two metal halves. The right acceleration point is achieved by matching the frequency of the voltage with the particle's cyclotron resonance frequency (only a function of charge, mass and strength of external magnetic field). When they reach the desired energy, a deflection

plate attracts the beam, changing its path from the circular one and directing it into a target or another further component. It is however required to take into account the relativistic effects which would lead to an adaptation of the RF field frequency or a time-dependent applied magnetic field.

A FFAG accelerator (fixed field alternating gradient) puts together the time-independent field of a cyclotron with the spatial gradient in this field such that the radius of curvature remains approximately constant. Therefore, it can accommodate stable orbits at a range of energies. The fixed field implies no synchronization issues, higher repetition rate and therefore higher average current. The accelerator is built from a sequence of identical cells, each one having alternating focusing and defocusing magnets.

To obtain the stable orbits, the key feature is the increase in the strength of the magnetic field with radius. This can be done by sticking to a power law  $r^k$ , where  $k$  is the field index in the scaling FFAGs (orbits of different energies have the same shape, but their size scales with the energy). As a consequence, this type of accelerator has the disadvantage of large aperture magnets. Relaxing the power law condition, the size of the orbits does not have such a large variation and the shapes become non-similar.

All of the above are linked together to form the basic principles behind the functioning of synchrotrons and FFAG accelerators.



Pure quadrupole,  $Nl$  turns/pole

Figure 1.4: Cross-section of a quadrupole magnet

## 1.4 Linear Beam Optics with Quadrupoles

A quadrupole magnet has four iron poles with hyperbolic contour. The field is linear with in the deviation from the axis:

$$B_z = -gx \quad (1)$$

$$B_x = -gz \quad (2)$$

In the air gap between the magnets (no iron or currents) we have

$$\nabla \times \mathbf{B} = 0 \quad (3)$$

Therefore the field can be written as the gradient of a potential which implies that the equipotentials are hyperbolas  $xz = const.$

$$\mathbf{B} = -\nabla V \quad (4)$$

$$V(x, y) = gxz \quad (5)$$

The gradient  $g$  and the current  $I$  through the coils can be related by one of Maxwell's equations

$$\oint \mathbf{H} \cdot d\mathbf{s} = nI \quad (6)$$

Using a certain path of integration and assuming  $\mu_r \gg 1$  inside the iron we obtain the following good approximation (where  $R$  is the shortest distance from the center to one of the hyperbolic poles)

$$g = \frac{2\mu_0 n I}{R^2} \quad (7)$$

Finally, the magnetic field is given by

$$\mathbf{B} = \frac{2\mu_0 n I}{R^2} \begin{pmatrix} -z \\ 0 \\ -x \end{pmatrix} \quad (8)$$

An important note is that this is a linear machine: the components of the Lorentz force are not coupled and therefore, the horizontal and vertical betatron oscillations are completely decoupled. For this field we can write the vector potential

$$\mathbf{A} = \begin{pmatrix} A_x \\ A_s \\ A_z \end{pmatrix} = \frac{g}{2} \begin{pmatrix} 0 \\ z^2 - x^2 \\ 0 \end{pmatrix} \quad (9)$$

where  $g$  is related to the quadrupole focusing strength  $k = \frac{e}{c p_0} \frac{dB_z}{dx}$ . The Hamiltonian for a charged particle in a magnetic field derived in Cartesian coordinates is

$$H = \sqrt{(mc^2)^2 + c^2(\mathbf{p} - e\mathbf{A})^2} \quad (10)$$

To carry out a transformation from the Cartesian coordinates to the local coordinates  $s$ ,  $x$  and  $z$ , we use a generating function of the third type

$$F_3(\boldsymbol{\pi}, s, x, z) = -\boldsymbol{\pi} \cdot (\mathbf{r}_0(s) + x\hat{\mathbf{x}} + y\hat{\mathbf{y}}) \quad (11)$$

In this equation  $\boldsymbol{\pi}$  is the old momentum from which the new canonical momentum  $\boldsymbol{\Pi}$  can be derived

$$\Pi_x = -\frac{\partial F_3}{\partial x} = \boldsymbol{\pi} \cdot \hat{\mathbf{x}} = \pi_x \quad (12)$$

$$\Pi_z = -\frac{\partial F_3}{\partial z} = \boldsymbol{\pi} \cdot \hat{\mathbf{z}} = \pi_z \quad (13)$$

$$\Pi_s = -\frac{\partial F_3}{\partial s} = \boldsymbol{\pi} \cdot \frac{d\mathbf{r}_0}{ds} = \boldsymbol{\pi} \cdot \hat{\mathbf{s}} = \pi_s \quad (14)$$

Using that  $A_x = 0, A_z = 0$ , the Hamiltonian becomes

$$H = c \left[ m^2 c^2 + \Pi_x^2 + \Pi_z^2 + (\Pi_s - eA_s)^2 \right]^{1/2} \quad (15)$$

Hamilton's equations are

$$\dot{s} = \frac{\partial \Pi_s}{\partial H}, \dot{\Pi}_s = -\frac{\partial \Pi_s}{\partial s}; \quad \dot{x} = \frac{\partial \Pi_x}{\partial H}, \dot{\Pi}_x = -\frac{\partial \Pi_x}{\partial x}; \quad \dot{z} = \frac{\partial \Pi_z}{\partial H}, \dot{\Pi}_z = -\frac{\partial \Pi_z}{\partial z};$$

The Hamiltonian is time-independent and it describes particle's motion with three degrees of freedom. We can lower the number of degrees of freedom

from three to two by using the constancy of  $H$  and changing the independent variable from  $t$  to  $s$ . We have that

$$x' = \frac{dx}{ds} = \frac{\dot{x}}{\dot{s}} = \left( \frac{\partial H}{\partial \Pi_x} \right) \left( \frac{\partial H}{\partial \Pi_s} \right)^{-1} = \frac{\partial(-\Pi_s)}{\partial \Pi_x} \quad (16)$$

This equation indicates that  $K = -\Pi_s$  becomes the new Hamiltonian with the conjugate coordinates  $x, \Pi_x; z, \Pi_z; t, -H$ . A similar approach also gives

$$\frac{d\Pi_x}{ds} = \frac{d\Pi_x/dt}{ds/dt} = \frac{-\partial H/\partial x}{\partial H/\partial \Pi_s} = \left( \frac{\partial \Pi_s}{\partial x} \right)_H = -\frac{\partial K}{\partial x} \quad (17)$$

Assuming that the particles travel at small angles from the nominal orbit, we consider the momenta along  $x$  and  $z$  small compared to the total momentum. The new Hamiltonian  $K$  can be approximated to

$$K = - \left[ \frac{H^2}{c^2} - \Pi_x^2 - \Pi_z^2 - m^2 c^2 \right]^{1/2} - eA_s \quad (18)$$

$$K \approx -p \left( 1 - \frac{\Pi_x^2}{2p^2} - \frac{\Pi_z^2}{2p^2} - eA_s \right) \quad (19)$$

where  $p(H) = \sqrt{H^2/c^2 - m^2 c^2}$  is the total kinetic momentum of a particle which for on-momentum particles becomes  $p_0$ . We can normalize the momenta,  $P_i = \Pi_i/p_0$ , and swap to a new Hamiltonian  $\mathcal{H} = K/p_0$  to preserve the structure of the equations, obtaining

$$\mathcal{H} \approx - \left( 1 - \frac{P_x^2}{2} - \frac{P_z^2}{2} \right) - \frac{k(s)}{2}(z^2 - x^2) \quad (20)$$

Using the results of (16) and (17) we get

$$x' = \frac{\partial \mathcal{H}}{\partial P_x} = P_x \quad (21)$$

$$x'' = \frac{dx'}{ds} = -\frac{\partial \mathcal{H}}{\partial x} = -k(s)x \quad (22)$$

Finally, **Hill's equations** are

$$x'' + k(s)x = 0 \quad (23)$$

$$z'' - k(s)z = 0 \quad (24)$$

Any linear differential equation, like Hill's equation, has solutions which can be traced from one point  $S_1$  to another  $S_2$  by a 2x2 transfer matrix

$$\begin{pmatrix} x(s_1) \\ x'(s_1) \end{pmatrix} = M_{21} \begin{pmatrix} x(s_2) \\ x'(s_2) \end{pmatrix} \quad (25)$$

For one lattice element such as a quadrupole,  $k(s) = constant$ . In this case, the solution to Hill's equation for the variable  $u = x, y$  is

$$u(s) = C(s)u_0 + S(s)u'_0 \quad (26)$$

Writing the solution in matrix form

$$\begin{pmatrix} u \\ u' \end{pmatrix} = \begin{pmatrix} C & S \\ C' & S' \end{pmatrix} \begin{pmatrix} u_0 \\ u'_0 \end{pmatrix} = M \begin{pmatrix} u_0 \\ u'_0 \end{pmatrix} \quad (27)$$

Therefore, we obtain the transfer matrices for a quadrupole magnet (focusing, defocusing)

$$M_{QF} = \begin{pmatrix} \cos(\sqrt{k}l) & \frac{1}{\sqrt{k}} \sin(\sqrt{k}l) \\ -\sqrt{k} \sin(\sqrt{k}l) & \cos(\sqrt{k}l) \end{pmatrix} \quad (28)$$

$$M_{DF} = \begin{pmatrix} \cosh(\sqrt{|k|}l) & \frac{1}{\sqrt{|k|}} \sinh(\sqrt{|k|}l) \\ -\sqrt{|k|} \sinh(\sqrt{|k|}l) & \cosh(\sqrt{|k|}l) \end{pmatrix} \quad (29)$$

A transfer matrix has always the determinant equal to 1 (it can be shown in a general case starting from the Twiss matrix). In the case of a quadrupole

$$|M_{QF}| = \cos^2 \phi + \sin^2 \phi = 1 \quad (30)$$

$$|M_{QD}| = \cosh^2 \phi - \sinh^2 \phi = 1 \quad (31)$$

To make the connection with the beam emittance (area of the beam in phase-space coordinates) we define the rms beam emittance and the  $\sigma$  - matrix as follows

$$\epsilon_{rms} = \sqrt{\sigma_x^2 \sigma_{x'}^2 - \sigma_{xx'}^2} \quad (32)$$

$$\sigma \equiv \begin{pmatrix} \sigma_x^2 & \sigma_{xx'}^2 \\ \sigma_{xx'}^2 & \sigma_{x'}^2 \end{pmatrix} = \langle (\langle \mathbf{y} \rangle - \langle \mathbf{y} \rangle) \rangle \langle (\langle \mathbf{y} \rangle - \langle \mathbf{y} \rangle)^\dagger \rangle \quad (33)$$

Under these definitions  $\epsilon_{rms} = \sqrt{\det \sigma}$ . The  $\sigma$  -matrix can also be traced with the aid of the transfer matrix

$$\sigma_2 = M_{21} \sigma_1 M_{21}^\dagger \quad (34)$$

Therefore the determinant of a transfer matrix being unity implies the emittance conservation:

$$\det(\sigma_2) = [\det(M_{21})]^2 \times \det(\sigma_1) = \det(\sigma_1) \Rightarrow \epsilon_{rms,2} = \epsilon_{rms,1} \quad (35)$$

## 1.5 Linear Beam Optics with Dipoles

A dipole magnet is used to bend the orbit. The field associated with it is  $\mathbf{B} = B(s)\hat{\mathbf{z}}$ . The function  $B(s)$  is such that it is not zero only inside the magnet and vanishes outside of it. For a constant field in a gap of height  $h$ , neglecting fringe fields and iron saturation, the following derivation is possible

$$\oint \mathbf{H} \cdot d\mathbf{s} = hH_0 + lH_E = nI \quad (36)$$

$$H_E = \frac{1}{\mu_r} H_0 \ll H_0 \quad (37)$$

$$\Rightarrow B_0 = \frac{\mu_0 n I}{h} \quad (38)$$

The radius of curvature is obtained from Newton's second law

$$\frac{mv^2}{\rho} = qvB \Rightarrow \frac{1}{\rho} = \frac{qB}{mv} \quad (39)$$

$$\rho = \frac{p}{eB} \quad (40)$$

The field can be represented by the vector potential

$$A_s = -B(s) \times \left(1 - \frac{x}{2\rho}\right) \quad (41)$$

$$A_x = A_z = 0 \quad (42)$$

The magnetic field obtained from this vector potential corresponds to the field of the dipole if we neglect the second order terms since the complete result has the form  $B_z \approx B(s) + O\left(\frac{x^2}{\rho^2}\right)$ . Because of the radius of curvature, the unit vector  $\hat{\mathbf{x}}$  is a function of  $s$ , i.e.  $\hat{\mathbf{x}}(s)$ . So the conjugate momentum  $\Pi_s$  becomes

$$\Pi_s = -\frac{\partial F_3}{\partial s} = \boldsymbol{\pi} \cdot \left( \frac{d\mathbf{r}_0}{ds} + x \frac{d\hat{\mathbf{x}}}{ds} \right) \quad (43)$$

$$= \boldsymbol{\pi} \cdot \left( \hat{\mathbf{s}} + \frac{x}{\rho} \hat{\mathbf{s}} \right) = \pi_s \left( 1 + \frac{x}{\rho} \right) \quad (44)$$

Therefore the Hamiltonian for the dipole field is

$$H = c \left[ m^2 c^2 + \Pi_x^2 \Pi_z^2 + \left( \frac{\Pi_s}{1 + x/\rho} - eA_s \right)^2 \right]^{1/2} \quad (45)$$

Following the same arguments as for the quadrupole magnet we change to a new "normalized" Hamiltonian  $\mathcal{H}$  which can be separated into  $z$  and  $x$

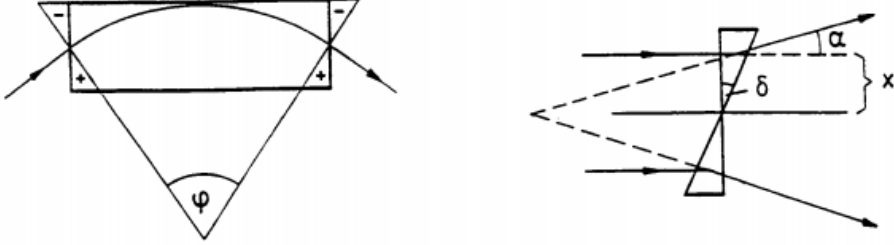


Figure 1.5: Dipole wedge treatment

components.

$$\mathcal{H} = - \left(1 + \frac{x}{\rho}\right) \left(1 - \frac{1}{2} P_x^2 - \frac{1}{2} P_z^2\right) - \frac{e}{p_0} A_s \left(1 + \frac{x}{\rho}\right) \quad (46)$$

$$\mathcal{H}_x \simeq \frac{1}{2} P_x^2 + \frac{K_x(s)}{s} x^2 \quad (47)$$

where  $K_x(s) = \frac{1}{\rho^2}$ . From this Hamiltonian we obtain the equations of motion, from which the one along  $\hat{\mathbf{x}}$  is non-trivial

$$x'' + \frac{1}{\rho^2} = 0 \quad (48)$$

Therefore the transfer matrix for a "hard edge" dipole (i.e. the magnet ends are perpendicular to the circular trajectory) is

$$M_x = \begin{pmatrix} \cos(l/\rho) & \rho \sin(l/\rho) \\ -\frac{1}{\rho} \sin(l/\rho) & \cos(l/\rho) \end{pmatrix} \quad (49)$$

A rectangular magnet can be derived from a sector magnet by superimposing at the entrance and exit a "magnetic wedge" of angle  $\delta = \phi/2$  (treating the edge as an impulse kick). The deflection angle in the magnetic wedge is

$$\alpha = \frac{\Delta l}{\rho} = \frac{x \tan \delta}{\rho} = \frac{x}{f} \quad (50)$$

It acts as a thin defocusing lens with focal length  $f = \frac{\rho}{\tan \delta}$  in the horizontal plane and as a focusing lens with the same strength in the vertical plane. The corresponding transfer matrix for this edge effect is ( "-" focusing "/" "+" defocusing )

$$M_{edge} = \begin{pmatrix} 1 & 0 \\ \pm \frac{1}{\rho} \tan \delta & 1 \end{pmatrix} \quad (51)$$

The total transfer matrix for the dipole magnet is obtained by multiplying the sector magnet matrix with the above matrix at the right and left. To

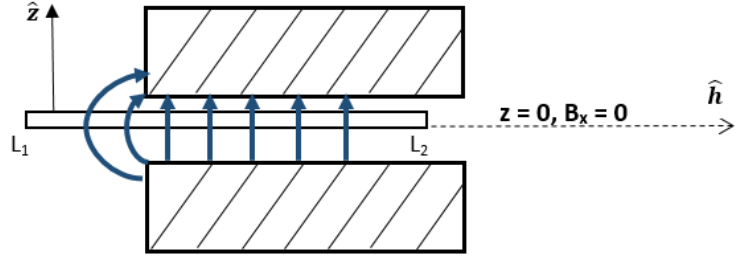


Figure 1.6: Edge integration path

show that the vertical focusing strength is the same requires a more detailed approach.

*Proof.*

$$\Delta z' = \frac{\Delta p_z}{p} = \frac{ev \int B(x)ds}{pv} = \frac{1}{\rho B} \int B_x ds \quad (52)$$

$$B_x = -B_h \sin \delta \quad B_x(z=0) = 0 \quad (53)$$

$$\Delta z' = -\frac{\sin \delta}{B\rho} \int B_h ds = -\frac{\tan \delta}{\rho B} \int (B_h \cos \delta) ds = -\frac{\tan \delta}{\rho B} \int_{L_1}^{L_2} \mathbf{B} \cdot d\mathbf{s}$$

$$\oint \mathbf{B} \cdot d\mathbf{s} = \int_{L_1}^{L_2} \mathbf{B} \cdot d\mathbf{s} - B_0 z = 0 \quad (54)$$

$$\Delta z' = -\frac{\tan \delta}{\rho B} \times (B_0 z) = -\frac{\tan \delta}{\rho} z \quad (55)$$

□

## 1.6 RF Cavities

An RF cavity is designed to provide a longitudinal electric field along the particle trajectory at a phase velocity equal to the particle velocity. Magnetic fields provide deflection, but no acceleration. The fields in an RF cavity are solutions to the wave equation

$$\nabla^2 \mathbf{E} - \frac{1}{c^2} \frac{\partial \mathbf{E}}{\partial t} = 0 \quad (56)$$

subjected to the boundary conditions:

- no tangential E-field,  $\hat{\mathbf{n}} \times \mathbf{E} = 0$ ;

- no normal magnetic field,  $\hat{\mathbf{n}} \cdot \mathbf{H} = 0$ .

The solution to the wave equation which has a longitudinal electric field is the TM (transverse magnetic) mode. Two of the general  $TM_{mnp}$  modes are generally used:  $TM_{0np}$  - monopoles modes that can couple to the beam and exchange energy; and  $TM_{1np}$  - dipole modes that can deflect the beam. The general TM modes in  $(r, \phi, s)$  coordinates have the following form (plus the  $e^{j\omega t}$  dependence)

$$E_s = Akr^2 J_m(k_r r) \cos(m\phi) \cos(k_s s) \quad (57)$$

$$E_r = -Ak_s k_r J_m'(k_r r) \cos(m\phi) \sin(k_s s) \quad (58)$$

$$E_\phi = A \left( \frac{mk_s}{r} \right) J_m(k_r r) \sin(m\phi) \sin(k_s s) \quad (59)$$

$$B_s = 0 \quad (60)$$

$$B_r = -jA \left( \frac{mk}{cr} \right) J_m(k_r r) \sin(m\phi) \cos(k_s s) \quad (61)$$

$$B_\phi = -jA \left( \frac{kk_r}{c} \right) J_m'(k_r r) \cos(m\phi) \cos(k_s s) \quad (62)$$

The  $k_{s,r}$  are the wave numbers in the longitudinal and radial modes, respectively and they satisfy

$$k = \frac{\omega}{c} = \sqrt{k_s^2 + k_r^2} \quad (63)$$

$$k_s = \frac{p\pi}{L}, \quad p = 0, 1, 2, \dots \quad (64)$$

$$k_{r,mn} = \frac{j_{mn}}{R}, \quad \text{where} \quad J_m(j_{mn}) = 0 \quad (65)$$

$$k_{mnp} = \sqrt{\frac{p^2\pi^2}{L^2} + \frac{j_{mn}^2}{c^2}} \quad (66)$$

The most simple example is the "pill box" cavity operated in  $TM_{010}$  mode. From Maxwell's equations

$$\frac{\partial^2 E_z}{\partial r^2} + \frac{1}{r} \frac{\partial E_z}{\partial r} = \frac{1}{c^2} \frac{\partial^2 E_z}{\partial t^2} \quad (67)$$

with the solution  $E_z(r) = E_0 J_0(\frac{\omega_0}{c} r) e^{-j\omega_0 t}$  where  $\omega_0 = \frac{2.405c}{R}$  and also  $E_r = E_\phi = 0$ . The accelerating voltage for charged particles is given by the integral

$$V_c = \left| \int_{-\infty}^{\infty} E_z(\rho = 0, z) e^{j\omega_0 z / \beta c} dz \right| \quad (68)$$

For the pill box cavity, this integral leads to the transit time factor T

$$V_c = E_0 \int_0^d e^{j\omega_0 z / \beta c} dz = E_0 d \cdot \text{sinc} \left( \frac{\omega_0 d}{\beta c} \right) = E_0 d \cdot T \quad (69)$$

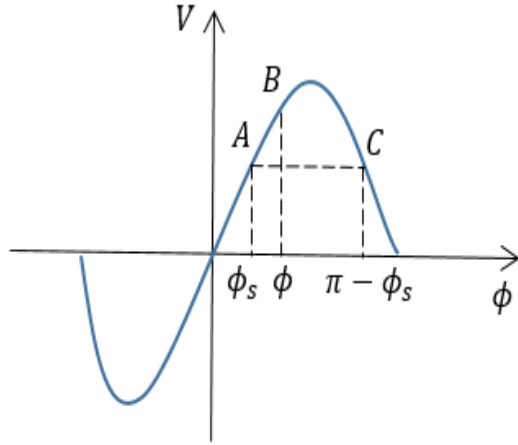


Figure 1.7: Longitudinal phase space

The condition for which the beam is longitudinally focusing (i.e. particles never lag too far behind the RF field) is generally referred as the "longitudinal phase space stability". This phase space is described by the coordinates of energy difference between the ideal, synchronous particle (i.e. it always arrives at the desired phase lag  $\phi_s$  behind the rising zero-crossing of the RF wave) and the phase lag  $\phi$ .

In this phase-space, a particle (B) is restored and oscillates about the stable phase (A) provided it does not reach and pass the point (C) where it receives less voltage than the synchronous particle. This is equivalent to  $\phi < \pi - \phi_s$ . The energy gain difference between a particle of general phase lag  $\phi$  and a synchronous particle is

$$\Delta E = E - E_s = TeV_0 (\sin \phi - \sin \phi_s) \quad (70)$$

If the revolution frequency  $f$  is higher for a higher momentum particle, the higher energy particle will arrive at the RF gap earlier ( $\phi < \phi_s$ ). Therefore, higher energy particles will receive less energy gain if the RF wave synchronous phase is chosen such that  $0 < \phi_s < \frac{\pi}{2}$ . In the case  $\frac{df}{d\Delta p} < 0$ , the phase stability requires  $\frac{\pi}{2} < \phi_s < \pi$ .

## 1.7 Sextupoles and Octopoles

A sextupole magnet consists of six magnetic poles set out in an arrangement of alternating north and south poles around a central axis. They are used to deal with chromaticity (change of the linear parameters of transverse motion of a single particle related with a change of the beam energy) and to damp the head-tail instability (a transverse instability in which the field generated by the head of a bunch exerts a force on the tail of the bunch, leading to unstable motion of the tail and breakup of the bunch). If the sextupole is placed in a region of non-zero dispersion, there exists a strength of the field for which the particles in a range of certain energies are focused at the same point. This counterbalances the tendency of the quadrupole lattice to disperse the beam (since off-momentum particles are incorrectly focused in a quadrupole).

An octupole magnet has further effects on a beam: it reduces the coupling between particles inducing Landau damping. This represents the disappearance of the coherent transverse collective instabilities due to tune spread.

# Week 2

In the following sections there are three models presented for the fringe field of a multipole. The first one deals with a straight multipole, while the second one treats a curved multipole, both starting with a power expansion for the magnetic field. The last model tries to be different by starting with a more compact functional form of the field which is then adapted to straight and curved geometries.

## 1.1 Fringe field models

(for a straight multipole)

Most accelerator modeling codes use the hard-edge model for magnets - constant Hamiltonian. Real magnets always have a smooth transition at the edges - fringe fields. To obtain a multipole description of a field we can apply the theory of analytic functions.

$$\nabla \cdot \mathbf{B} = 0 \Rightarrow \exists \quad \mathbf{A} \quad \text{with} \quad \mathbf{B} = \nabla \times \mathbf{A} \quad (71)$$

$$\nabla \times \mathbf{B} = 0 \Rightarrow \exists \quad V \quad \text{with} \quad \mathbf{B} = -\nabla V \quad (72)$$

Assuming that  $A$  has only a non-zero component  $A_s$  we get

$$B_x = -\frac{\partial V}{\partial x} = \frac{\partial A_s}{\partial y} \quad (73)$$

$$B_y = -\frac{\partial V}{\partial y} = -\frac{\partial A_s}{\partial x} \quad (74)$$

These equations are just the Cauchy-Riemann conditions for an analytic function  $\tilde{A}(z) = A_s(x, y) + iV(x, y)$ . So the complex potential is an analytic function and can be expanded as a power series

$$\tilde{A}(z) = \sum_{n=0}^{\infty} \kappa_n z^n, \quad \kappa_n = \lambda_n + i\mu_n \quad (75)$$

with  $\lambda_n, \mu_n$  being real constants. It is practical to express the field in cylindrical coordinates  $(r, \varphi, s)$

$$x = r \cos \varphi \quad y = r \sin \varphi \quad (76)$$

$$z^n = r^n (\cos n\varphi + i \sin n\varphi) \quad (77)$$

From the real and imaginary parts of equation () we obtain

$$V(r, \varphi) = \sum_{n=0}^{\infty} r^n (\mu_n \cos n\varphi + \lambda_n \sin n\varphi) \quad (78)$$

$$A_s(r, \varphi) = \sum_{n=0}^{\infty} r^n (\lambda_n \cos n\varphi - \mu_n \sin n\varphi) \quad (79)$$

Taking the gradient of  $-V(r, \varphi)$  we obtain the multipole expansion of the azimuthal and radial field components, respectively

$$B_\varphi = -\frac{1}{r} \frac{\partial V}{\partial \varphi} = -\sum_{n=0}^{\infty} nr^{n-1} (\lambda_n \cos n\varphi - \mu_n \sin n\varphi) \quad (80)$$

$$B_r = -\frac{\partial V}{\partial r} = -\sum_{n=0}^{\infty} nr^{n-1} (\mu_n \cos n\varphi + \lambda_n \sin n\varphi) \quad (81)$$

Furthermore, we introduce the normal multipole coefficient  $b_n$  and skew coefficient  $a_n$  defined with the reference radius  $r_0$  and the magnitude of the field at this radius  $B_0$  (these coefficients can be a function of  $s$  in a more general case as it is presented further on).

$$b_n = -\frac{n\lambda_n}{B_0} r_0^{n-1} \quad a_n = \frac{n\mu_n}{B_0} r_0^{n-1} \quad (82)$$

$$B_\varphi(r, \varphi) = B_0 \sum_{n=1}^{\infty} (b_n \cos n\varphi + a_n \sin n\varphi) \left( \frac{r}{r_0} \right)^{n-1} \quad (83)$$

$$B_r(r, \varphi) = B_0 \sum_{n=1}^{\infty} (-a_n \cos n\varphi + b_n \sin n\varphi) \left( \frac{r}{r_0} \right)^{n-1} \quad (84)$$

To obtain a model for the fringe field of a straight multipole, a proposed starting solution for a non-skew magnetic field is

$$V = \sum_{n=1}^{\infty} V_n(r, z) \sin n\varphi \quad (85)$$

$$V_n = \sum_{k=0}^{\infty} C_{n,k}(z) r^{n+2k} \quad (86)$$

It is straightforward to derive a relation between coefficients

$$\nabla^2 V = 0 \Rightarrow \frac{1}{r} \frac{\partial}{\partial r} \left( r \frac{\partial V_n}{\partial r} \right) + \frac{\partial^2 V_n}{\partial z^2} = \frac{n^2 V_n}{r^2} = 0 \quad (87)$$

$$V_n = \sum_{k=0}^{\infty} C_{n,k}(z) r^{n+2k} \quad (88)$$

$$\Rightarrow \sum_{k=0}^{\infty} \left[ r^{n+2(k-1)} [(n+2k)^2 - n^2] C_{n,k}(z) + r^{n+2k} \frac{\partial^2 C_{n,k}(z)}{\partial z^2} \right] = 0 \quad (89)$$

By identifying the term in front of the same powers of  $r$  we obtain the recurrence relation

$$C_{n,k}(z) = -\frac{1}{4k(n+k)} \frac{d^2 C_{n,k-1}}{dz^2}, \quad k = 1, 2, \dots \quad (90)$$

The solution of the recursion relation becomes

$$C_{n,k}(z) = (-1)^k \frac{n!}{2^{2k} k! (n+k)!} \frac{d^{2k} C_{n,0}(z)}{dz^{2k}} \quad (91)$$

Therefore

$$V_n = - \left( \sum_{k=0}^{\infty} (-1)^{k+1} \frac{n!}{2^{2k} k! (n+k)!} C_{n,0}^{(2k)}(z) r^{2k} \right) r^n \quad (92)$$

The transverse components of the field are

$$B_r = \sum_{n=1}^{\infty} g_{rn} r^{n-1} \sin n\varphi \quad (93)$$

$$B_\varphi = \sum_{n=1}^{\infty} g_{\varphi n} r^{n-1} \cos n\varphi \quad (94)$$

where the following gradients determine the entire potential and can be deduced from the function  $C_{n,0}(z)$  once the harmonic  $n$  is fixed.

$$g_{rn}(r, z) = \sum_{k=0}^{\infty} (-1)^{k+1} \frac{n!(n+2k)}{2^{2k} k! (n+k)!} C_{n,0}^{(2k)}(z) r^{2k} \quad (95)$$

$$g_{\varphi n}(r, z) = \sum_{k=0}^{\infty} (-1)^{k+1} \frac{n!n}{2^{2k} k! (n+k)!} C_{n,0}^{(2k)}(z) r^{2k} \quad (96)$$

The z-directed component of the field can be expressed in a similar form

$$B_z = -\frac{\partial V}{\partial z} = \sum_{n=1}^{\infty} g_{zn} r^n \sin n\varphi \quad (97)$$

$$g_{zn} = \sum_{k=0}^{\infty} (-1)^{k+1} \frac{n!}{2^{2k} k! (n+k)!} C_{n,0}^{2k+1} r^{2k} \quad (98)$$

The gradient functions  $g_{rn}, g_{\varphi n}, g_{zn}$  are obtained from

$$B_{r,n} = -\frac{\partial V_n}{\partial r} \sin n\varphi = g_{rn} r^{n-1} \sin n\varphi \quad (99)$$

$$B_{\varphi,n} = -\frac{n}{r} V_n \cos n\varphi = g_{\varphi n} r^{n-1} \cos n\varphi \quad (100)$$

$$B_{z,n} = -\frac{\partial V_n}{\partial z} \sin n\varphi = g_{zn} r^n \sin n\varphi \quad (101)$$

One preferred model to approximate the gradient profile on the central axis is the k-parameter Enge function

$$C_{n,0}(z) = \frac{G_0}{1 + \exp[P(d(z))]}, \quad G_0 = \frac{B_0}{r_0^{n-1}} \quad (102)$$

$$P(d) = C_0 + C_1 \left( \frac{d}{\lambda} \right) + C_2 \left( \frac{d}{\lambda} \right)^2 + \cdots + C_{k-1} \left( \frac{d}{\lambda} \right)^{k-1} \quad (103)$$

where  $d(z)$  is the distance to the field boundary and  $\lambda$  characterizes the fringe field length.

## 1.2 Fringe field of a curved multipole

(fixed radius)

We consider the Frenet-Serret coordinate system  $(\hat{\mathbf{x}}, \hat{\mathbf{s}}, \hat{\mathbf{z}})$  with the radius of curvature  $\rho$  constant and the scale factor  $h_s = 1 + x/\rho$ . A conversion to these coordinates implies that

$$\nabla \cdot \mathbf{B} = \frac{1}{h_s} \left[ \frac{\partial(h_s B_x)}{\partial x} + \frac{\partial B_s}{\partial s} + \frac{\partial(h_s B_z)}{\partial z} \right] \quad (104)$$

$$\nabla \times \mathbf{B} = \frac{1}{h_s} \left[ \frac{\partial B_z}{\partial s} - \frac{\partial(h_s B_s)}{\partial z} \right] \hat{\mathbf{x}} + \left[ \frac{\partial B_x}{\partial z} - \frac{\partial B_z}{\partial x} \right] \hat{\mathbf{s}} + \frac{1}{h_s} \left[ \frac{\partial(h_s B_s)}{\partial x} - \frac{\partial B_x}{\partial s} \right] \hat{\mathbf{z}}$$

To simplify the problem, consider multipoles with mid-plane symmetry, i.e.

$$b_z(z) = B_z(-z) \quad B_x(z) = -B_x(-z) \quad B_s(z) = -B_s(-z) \quad (105)$$

The most general form of the expansion is

$$B_z = \sum_{i,k=0}^{\infty} b_{i,k} x^i z^{2k} \quad (106)$$

$$B_x = z \sum_{i,k=0}^{\infty} a_{i,k} x^i z^{2k} \quad (107)$$

$$B_s = z \sum_{i,k=0}^{\infty} c_{i,k} x^i z^{2k} \quad (108)$$

Maxwell's equations  $\nabla \cdot \mathbf{B} = 0$  and  $\nabla \times \mathbf{B} = 0$  in the above coordinates yield

$$\frac{\partial}{\partial x} ((1 + x/\rho) B_x) + \frac{\partial B_s}{\partial s} + (1 + x/\rho) \frac{\partial B_z}{\partial z} = 0 \quad (109)$$

$$\frac{\partial B_z}{\partial s} = (1 + x/\rho) \frac{\partial B_s}{\partial z} \quad (110)$$

$$\frac{\partial B_x}{\partial z} = \frac{\partial B_z}{\partial s} \quad (111)$$

$$\frac{\partial B_x}{\partial s} = \frac{\partial}{\partial x} ((1 + x/\rho) B_s) \quad (112)$$

The substitution of (106), (107) and (108) into Maxwell's equations allows for the derivation of recursion relations. (111) gives

$$\sum_{i,k=0}^{\infty} a_{i,k} (2k+1) x^i z^{2k} = \sum_{i,k=0}^{\infty} b_{i,k} i x^{i-1} z^{2k} \quad (113)$$

Equating the powers in  $x^i z^{2k}$

$$a_{i,k} = \frac{i+1}{2k+1} b_{i+1,k} \quad (114)$$

A similar result is obtained from (112)

$$\sum_{i,k=0}^{\infty} \partial_s b_{i,k} x^i z^{2k} = \left(1 + \frac{x}{\rho}\right) \sum_{i,k=0}^{\infty} c_{i,k} (2k+1) x^i z^{2k} \quad (115)$$

$$\Rightarrow c_{i,k} + \frac{1}{\rho} c_{i-1,k} = \frac{1}{2k+1} \partial_s b_{i,k} \quad (116)$$

The last equation from  $\nabla \times \mathbf{B} = 0$  should be consistent with the two recursion relations obtained. (110) implies

$$\sum_{i,k=0}^{\infty} \left[ \frac{i+1}{\rho} c_{i,k} x^i + c_{i,k} i x^{i-1} \right] z^{k+1} = \sum_{i,k=0}^{\infty} \partial_s a_{i,k} x^i z^{2k} \quad (117)$$

$$\Rightarrow \frac{\partial_s a_{i,k}}{i+1} = \frac{1}{\rho} c_{i,k} + c_{i+1,k} \quad (118)$$

This results follows directly from (114) and (116); therefore the relations are consistent. Furthermore, the last required relations is obtained from the divergence of  $\mathbf{B}$

$$\begin{aligned} & \sum_{i,k=0}^{\infty} \left[ \frac{a_{i,k} x^i z^{2k+1}}{\rho} + i a_{i,k} x^{i-1} z^{2k+1} + \frac{i a_{i,k} x^i z^{2k+1}}{\rho} \right] + \\ & + \sum_{i,k=0}^{\infty} \left[ \partial_s c_{i,k} x^i z^{2k+1} + 2k b_{i,k} x^i z^{2k-1} + \frac{2k}{\rho} b_{i,k} x^{i+1} z^{2k-1} \right] = 0 \end{aligned} \quad (119)$$

$$\Rightarrow \partial_s c_{i,k} + \frac{2(k+1)}{\rho} b_{i-1,k+1} + 2(k+1)b_{i,k+1} + \frac{1}{\rho} a_{i,k} + (i+1)a_{i+1,k} + \frac{1}{\rho} a_{i,k} = 0$$

Using the relation (114) to replace the  $a$  coefficients with  $b$ 's we arrive at

$$\partial_s c_{i,k} + \frac{(i+1)^2}{\rho(2k+1)} b_{i+1,k} + \frac{(i+1)(i+2)}{2k+1} b_{i+2,k} + \frac{2(k+1)}{\rho} b_{i-1,k+1} + 2(k+1)b_{i,k+1} = 0 \quad (120)$$

All the coefficients above can be determined recursively provided the field  $B_z$  can be measured at the mid-plane in the form

$$B_z(z=0) = B_{0,0} + B_{1,0}x + B_{2,0}x^2 + B_{3,0}x^3 + \dots \quad (121)$$

where  $B_{i,0}$  are functions of  $s$  and they can model the fringe field for each multipole term  $x^n$ . As an example, for a dipole magnet, the  $B_{1,0}$  function can be model as an Enge function or  $\tanh$ .

### 1.3 Fringe field of a curved multipole

*(variable radius of curvature)*

The difference between this case and the above is that  $\rho$  is now a function of  $s$ ,  $\rho(s)$ . We can obtain the same result starting with the same functional forms for the field (106), (107), (108). The result of the previous section also holds in this case since no derivative  $\frac{\partial}{\partial s}$  is applied to the scale factor  $h_s$ . However the expression for  $h_s$  changes. This will be treated differently later. If the radius of curvature is set to be proportional to the dipole field observed by some reference particle that stays in the centre of the dipole

$$1/\rho(s) \propto B(z=0, x=0, s) = B_x(z=0, x=0) = b_{0,0}(s) \quad (122)$$

### 1.4 Fringe field of a multipole

*This is a different, more compact treatment*

The derivation is more clear if we gather the variables together in functions. We assume again mid-plane symmetry and that the z-component of the field in the mid-plane has the form

$$B_z(x, z=0, s) = T(x)S(s) \quad (123)$$

where  $T(s)$  is the transverse field profile and  $S(s)$  is the fringe field. One of the requirements of the symmetry is that  $B_z(z) = B_z(-z)$  which using a

scalar potential  $\psi$  requires  $\frac{\partial\psi}{\partial z}$  to be an even function in  $z$ . Therefore,  $\psi$  is an odd function in  $z$  and can be written as

$$\psi = zf_0(x, s) + \frac{z^3}{3!}f_1(x, s) + \frac{z^5}{5!}f_2(x, s) + \dots \quad (124)$$

The given transverse profile requires that  $f_0(x, s) = T(x)S(s)$ , while  $\nabla^2\psi = 0$  follows from Maxwell's equations as usual, more explicitly

$$\frac{\partial}{\partial x} \left( h_s \frac{\partial\psi}{\partial x} \right) + \frac{\partial}{\partial s} \left( \frac{1}{h_s} \frac{\partial\psi}{\partial s} \right) + \frac{\partial}{\partial z} \left( h_s \frac{\partial\psi}{\partial z} \right) = 0 \quad (125)$$

For a straight multipole  $h_s = 1$ . Laplace's equation becomes

$$\sum_{n=0} \frac{z^{2n+1}}{(2n+1)!} [\partial_x^2 f_n(x, s) + \partial_s^2 f_n(x, s)] + \sum_{n=1} f_n(x, s) \frac{z^{n-1}}{(n-1)!} = 0 \quad (126)$$

By equating powers of  $z$  we obtain the recursion relation

$$f_{n+1}(x, s) = -(\partial_x^2 + \partial_s^2) f_n(x, s) \quad (127)$$

The general expression for any  $f_n(x, s)$  is then obtained from the mid-plane field by

$$f_n(x, s) = (-1)^n (\partial_x^2 + \partial_s^2)^n f_0(x, s) \quad (128)$$

$$f_n(x, s) = (-1)^n \sum_{i=0}^n \binom{n}{i} T^{(2i)}(x) S^{(2n-2i)}(s) \quad (129)$$

For a curved multipole of constant radius  $h_s = 1 + \frac{x}{\rho}$  with  $\rho = const.$  The corresponding Laplace's equation is

$$\left( \frac{1}{\rho h_s} \partial_x + \partial_x^2 + \partial_z^2 + \frac{\partial_s^2}{h_s^2} \right) \psi = 0 \quad (130)$$

Again we substitute with the functional form of the potential to get the recursion

$$f_{n+1}(x, s) = - \left[ \frac{1}{\rho + x} \partial_x + \partial_x^2 + \frac{\partial_s^2}{(1+x/\rho)^2} \right] f_n(x, s) \quad (131)$$

$$f_n(x, s) = (-1)^n \left[ \frac{1}{\rho + x} \partial_x + \partial_x^2 + \frac{\partial_s^2}{(1+x/\rho)^2} \right]^n f_0(x, s) \quad (132)$$

Finally consider what changes for  $\rho = \rho(s)$ . An observation has to be made here: because of the variable radius, the scale factor  $h_s$  becomes

$$h_s = \left[ \left( \frac{\partial\rho}{\partial s} \right)^2 + \left( 1 + \frac{x}{\rho} \right)^2 \right]^{1/2} \quad (133)$$

Laplace's equation gives

$$\left[ \frac{\partial_x(h_s)}{h_s} \partial_x + \partial_x^2 + \partial_z^2 + \frac{\partial_s^2}{h_s^2} + \partial_s \left( \frac{1}{h_s} \right) \frac{\partial_s}{h_s} \right] \psi = 0 \quad (134)$$

The last step is again the substitution to get

$$f_{n+1}(x, s) = - \left[ \frac{\partial_x(h_s)}{h_s} \partial_x + \partial_x^2 + \frac{\partial_s^2}{h_s^2} + \partial_s \left( \frac{1}{h_s} \right) \frac{\partial_s}{h_s} \right] f_n(x, s) \quad (135)$$

$$f_n(x, s) = (-1)^n \left[ \frac{\partial_x(h_s)}{h_s} \partial_x + \partial_x^2 + \frac{\partial_s^2}{h_s^2} + \partial_s \left( \frac{1}{h_s} \right) \frac{\partial_s}{h_s} \right]^n f_0(x, s) \quad (136)$$

If the radius of curvature is inversely proportional to the dipole field in the centre of the multipole (the dipole component of the transverse field is a constant  $T_{dipole}(x) = B_0$  multiplied by  $S(s)$ ) then

$$\rho(s) = \frac{\rho(0)}{S(s)} \quad (137)$$

# Weeks 3 and 4

## 1.1 Multipole Models in OPAL

The current version of the OPAL library has the possibility to represent a multipole of arbitrary order by setting the normal and skew coefficients of the field. However, the only model that includes fringe fields is that of a dipole (both straight and sector magnet), using the Enge function with 6 parameters. All the others higher multipoles are represented as hard edge magnets.

The figure 1.8 shows the normalised vertical component of the magnetic field on the mid-plane where  $x$  is the relative distance from the reference trajectory measured radially and "phi" is the angle along the circular trajectory. This component has the expected behaviour (soft edges and constant value everywhere inside the magnet). The other two components are identically zero everywhere on the mid-plane.

An analysis of the field map off the mid-plane shows some unexpected peculiarities. The figures 1.9 and 1.10 represent the components of the field off the mid-plane. The sudden change in the pattern is caused by reaching the edge of the aperture and entering the material of the magnet. It seems like inside the material the code is calculating the fringe fields even if the field inside the magnet is not calculated. The vertical component  $\mathbf{B}_z$  shows deviations in the form of spikes at the regions where the fringe field reaches the value of the central field. We will show later that these deviations have consequences on the value of the curl of the field. The  $\mathbf{B}_x$  component was expected to be symmetric, but it is non-zero only at the exit edge of the magnet. The  $\mathbf{B}_y$  component is symmetric and increases as we get further away from the mid-plane.

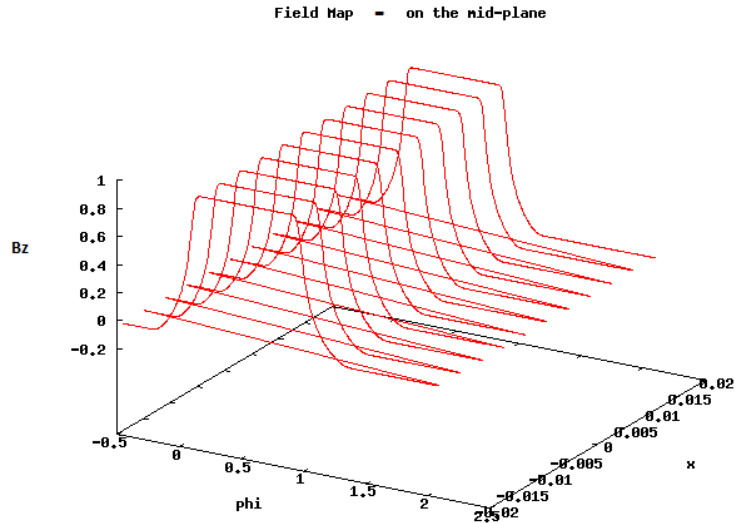


Figure 1.8: Vertical component of the field on mid-plane

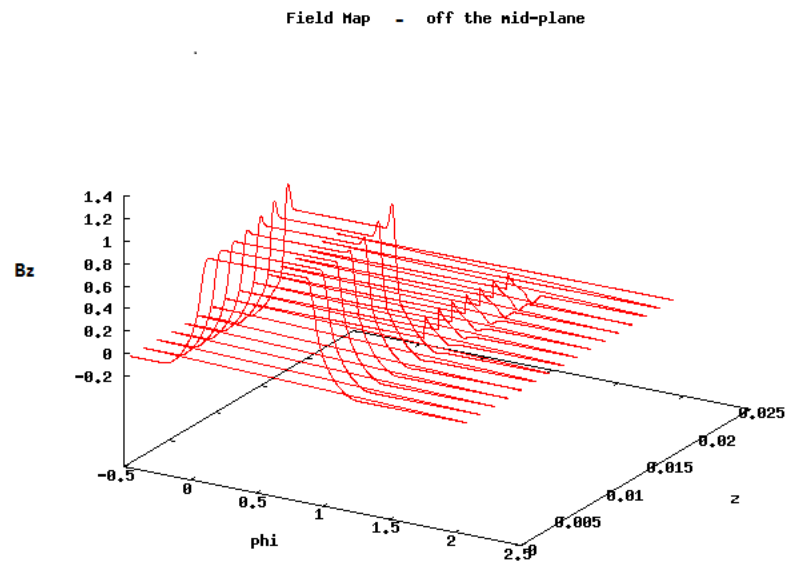


Figure 1.9: figure  
Vertical component of the field off mid-plane

## 1.2 Maxwell's equations

We built a unit test for Maxwell's equations and run it for the field of the dipole. Firstly, the value of the divergence of the field is close to zero

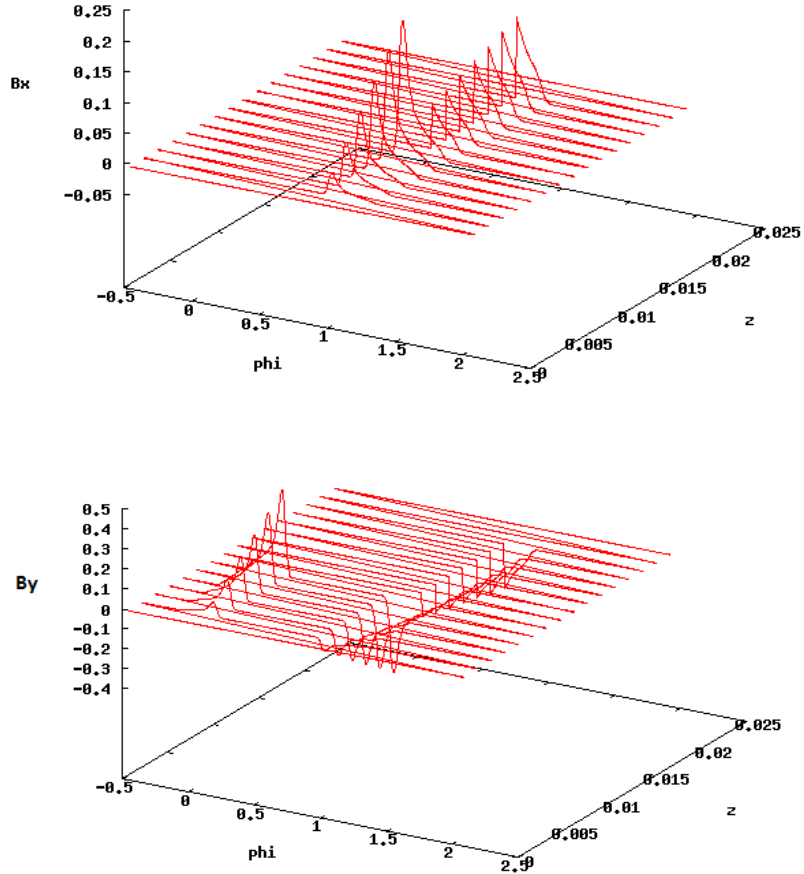


Figure 1.10: Horizontal components of the field off mid-plane

(expected since the field is mainly constant in space) as shown by figure 1.11 and 1.12 where the values are not normalised. For the parameters chosen to describe the magnet (length, aperture, reference radius, design energy of the particles, bending angle of 30 degrees) the value of the field is of order  $10^6$  units. We can therefore imply that when normalised the divergence of the field is indeed close to zero even off the mid-plane.

Secondly, the normalised absolute value of the curl of the field is 35 times higher than unity on the mid-plane and 80 times higher off the mid-plane - figure 1.13 and figure 1.14. The regions of non-uniformity are the end fields as expected. The spike-shaped deviations and the horizontal components of the field are believed to cause this behaviour. Since the curl of the field is non-zero, the model is not completely realistic.

We tried to refine the existing model by including more terms in some of

**DivB on the mid-plane**

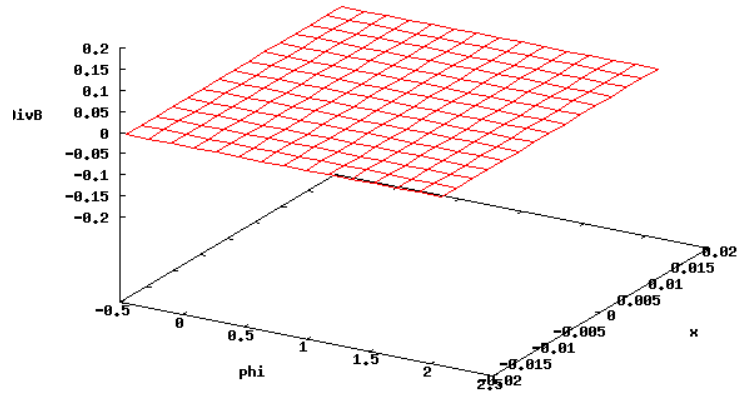


Figure 1.11: Divergence of the field on mid-plane

**DivB off the mid-plane**

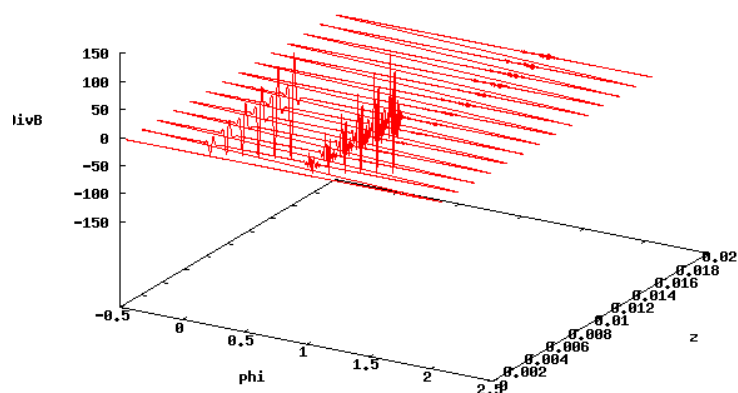


Figure 1.12: Divergence of the field off mid-plane

the expansions used in the code. As shown in the figure 1.15 these changes eliminate the corner deviations but introduces irregularities near the origin of the Enge functions used in the end fields. Furthermore, the normalised absolute value of the curl of the field drops by a factor of 10 (figure 1.16), still not good enough to accept it as a realistic model.

**CurlB on the mid-plane**

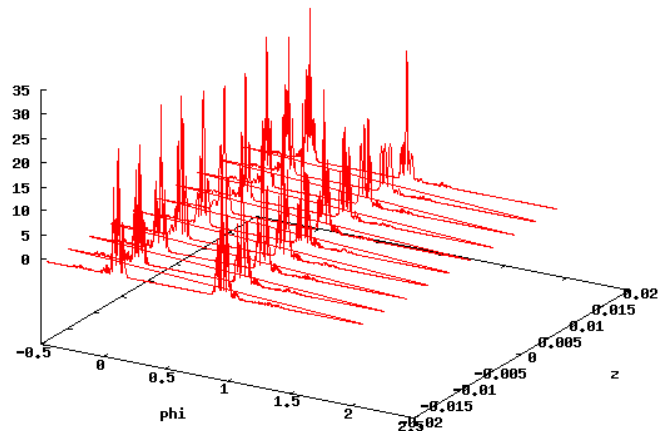


Figure 1.13:  $|\nabla \times \mathbf{B}|$  on the mid-plane

**CurlB off the mid-plane**

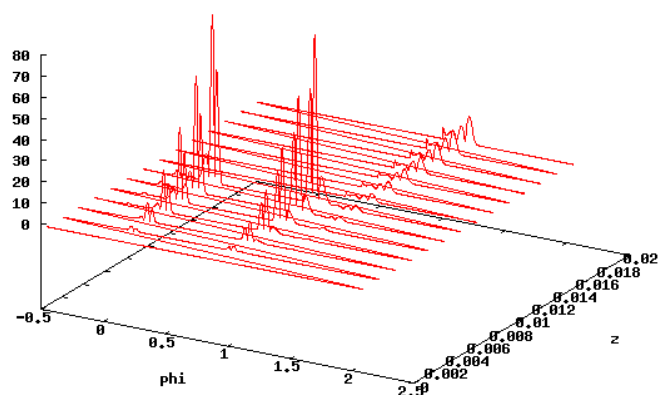


Figure 1.14:  $|\nabla \times \mathbf{B}|$  off the mid-plane

As mentioned before, the higher multipole models do not include fringe fields (for example figure 1.17 shows the field map of a quadrupole in OPAL).

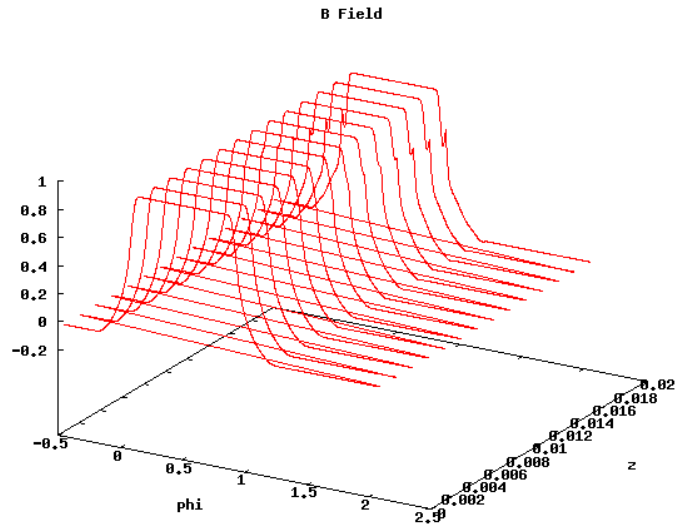


Figure 1.15: Vertical component of the refined field off mid-plane

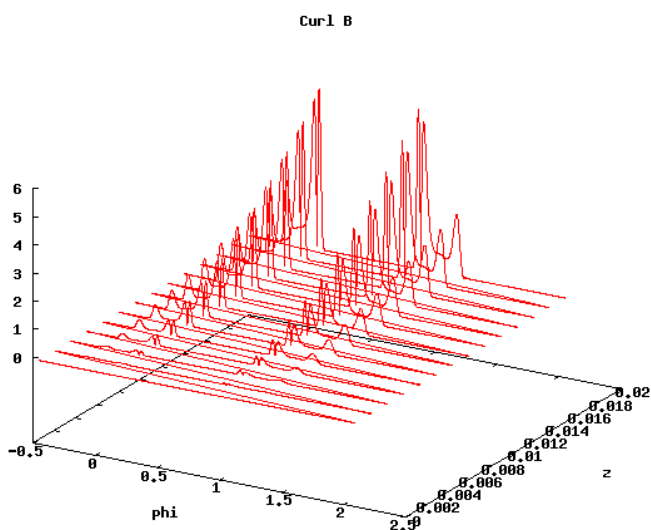


Figure 1.16:  $|\nabla \times \mathbf{B}|$  off the mid-plane for the refined-field

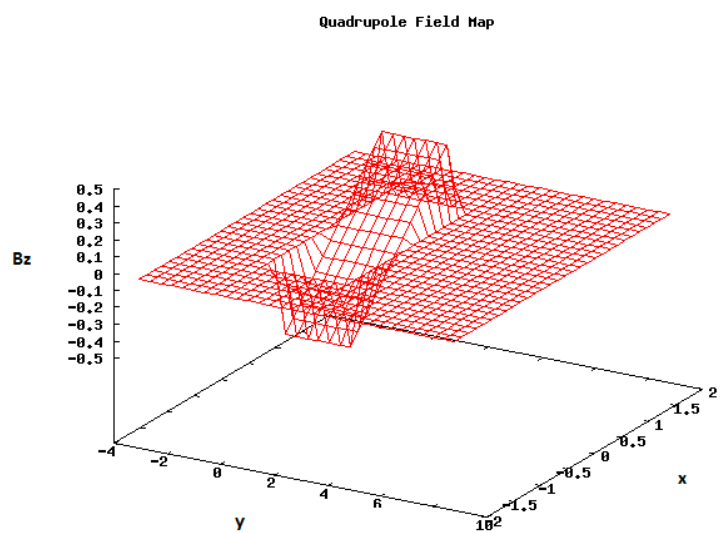


Figure 1.17: Vertical component in a quadrupole

# Weeks 5

## 1.1 New Multipole Model in OPAL

Since the pre-existing multipole model in OPAL only supports fringe fields for dipoles and does not offer the possibility to use combined function magnets, we decided to implement our new model. The field expansion used in this implementation follows the description of section 1.4 for a straight multipole.

The new element is called "MultipoleT" and has the following attributes (note - the model is extended later, some of these attributes are changed, see next chapter): L - the length of the magnet (inherited from the component base this is the length of the central field), VAPERT and HAPERT - the dimensions of the aperture (currently this element only support a rectangular aperture), FRINGELEN - the length of the end fields, MAXFORDER - the number of terms used in the field expansion (more precisely in the scalar magnetic potential  $\psi$ ), TP - the transverse profile. The TP attribute is a vector consisting of the derivatives of the field expansion in the mid-plane. Referring to section 1.4, TP contains the derivatives of the transverse profile  $T(x)$ .

To test the functionality of this model we built a simple lattice consisting of 24 dipoles. We successfully found a closed circular orbit (figure 1.18) and run the tracking code multiple times for different particle energies or trajectory radii (figure 1.19 shows an open orbit).

The fringe fields can be observed at the ends of each dipole. Additional care needs to be taken when setting the length of the fringe fields. For small fringe fields, the values of the field start to diverge when the aperture is increased over a certain threshold. This aspect is shown in one of the following sections.

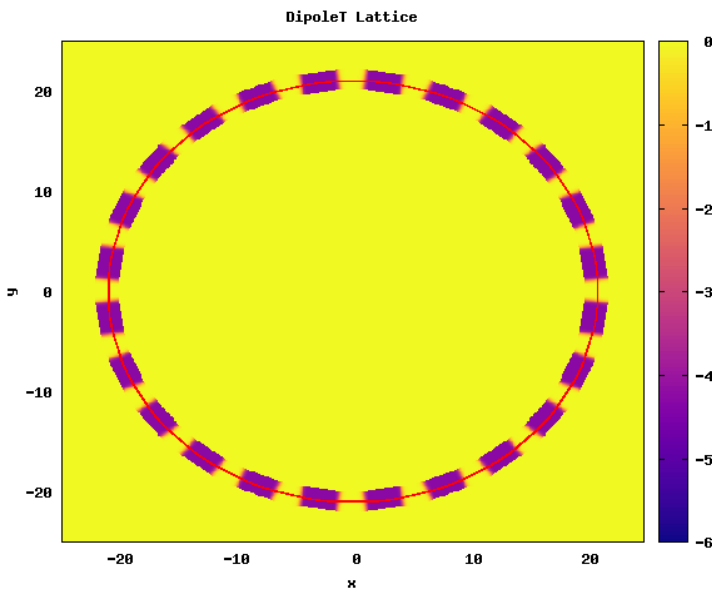


Figure 1.18: Closed orbit in a DipoleT lattice

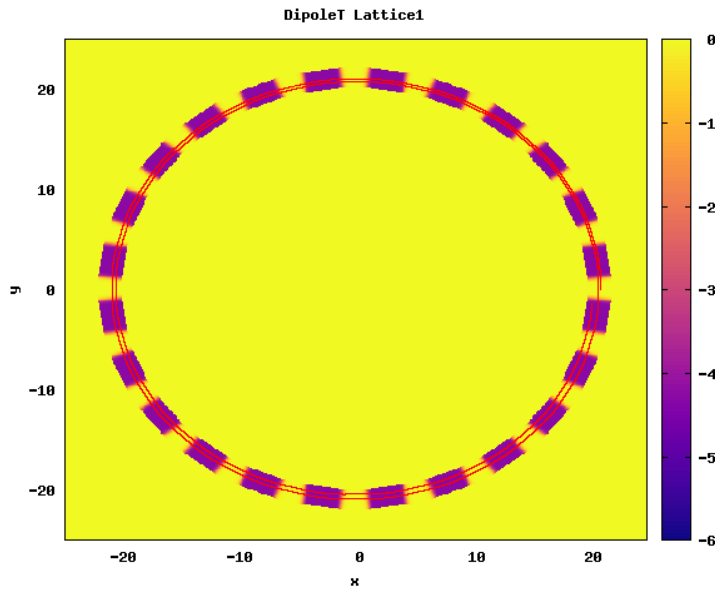


Figure 1.19: Open orbit in a DipoleT lattice

## 1.2 Maxwell's laws

Following the same procedure as for the pre-existing model, we wrote a unit test to make sure that the MultipoleT model satisfies Maxwell's laws. The

field for a dipole is shown in figure 1.20 (vertical component on the midplane, the other two components being identically zero) and figures 1.21 and 1.22 (off the mid-plane, the third component  $B_x$  being zero everywhere).

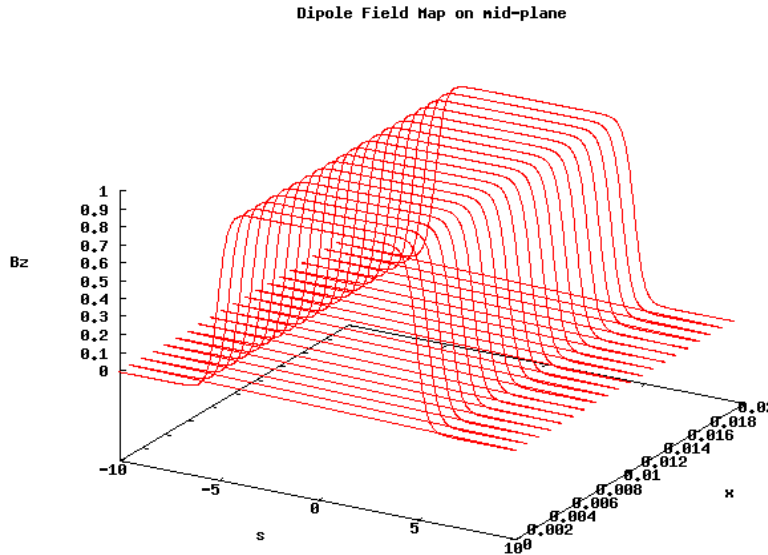


Figure 1.20: DipoleT field on mid-plane

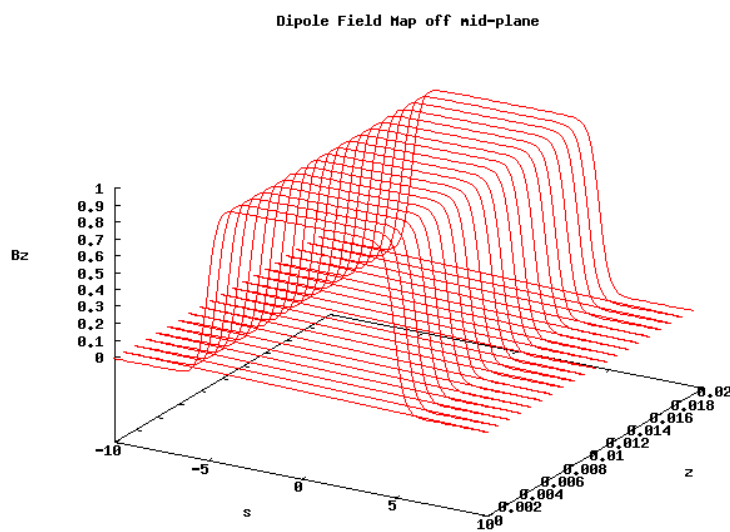


Figure 1.21: DipoleT field off mid-plane

The divergence and curl of the field are shown in figures 1.23, 1.24 and 1.25. While the divergence of  $\mathbf{B}$  is exactly zero everywhere, the curl shows some noise. This is most probably due to the precision in the calculation of

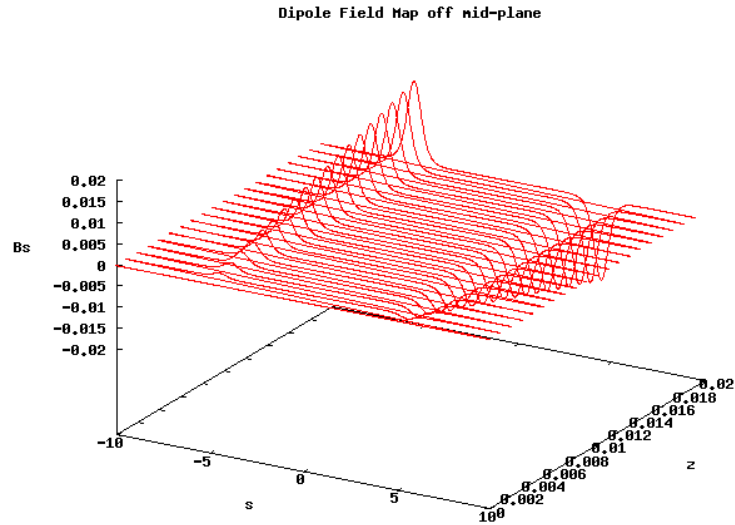


Figure 1.22: DipoleT field off mid-plane

derivatives. However, the noise is 10 orders of magnitude smaller than the field. Thus, we conclude that Maxwell's laws are obeyed.

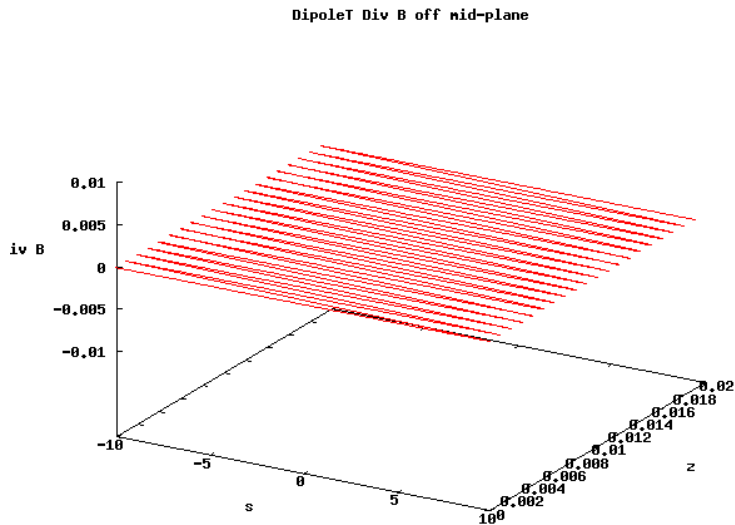


Figure 1.23: Divergence of the field off mid-plane

We also tested the MultipoleT element with the configuration of a quadrupole (the field is shown by figure 1.26). The unit test showed that Maxwell's equations are also satisfied by the quadrupole as seen in figures 1.27 and 1.28.

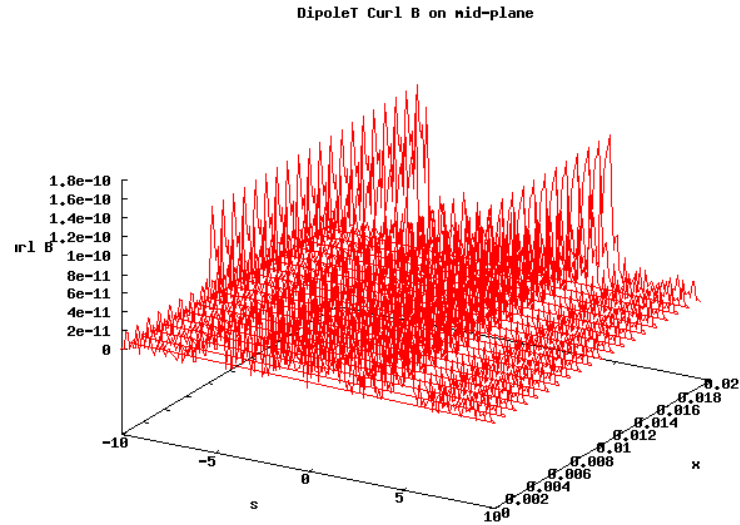


Figure 1.24:  $|\nabla \times \mathbf{B}|$  on the mid-plane

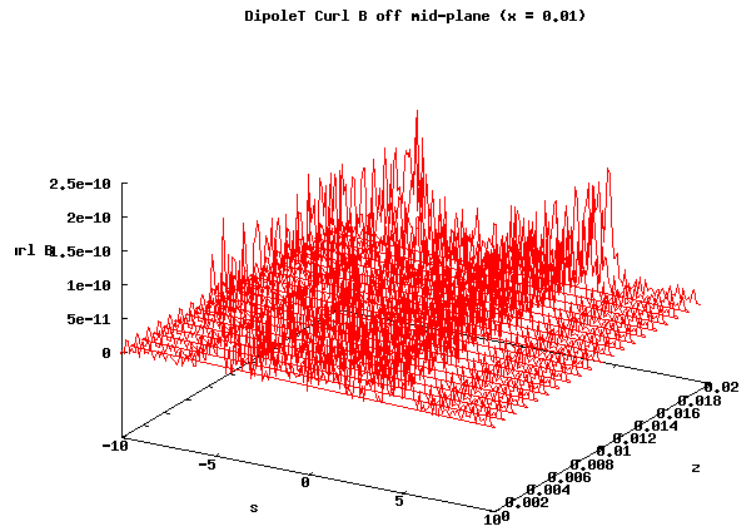


Figure 1.25:  $|\nabla \times \mathbf{B}|$  off the mid-plane

### 1.3 Convergence Studies

As mentioned in a previous section, the values of the aperture for which the field does not diverge is highly dependent on the length of the fringe fields. A smaller fringe field implies higher derivatives of the end fields. In

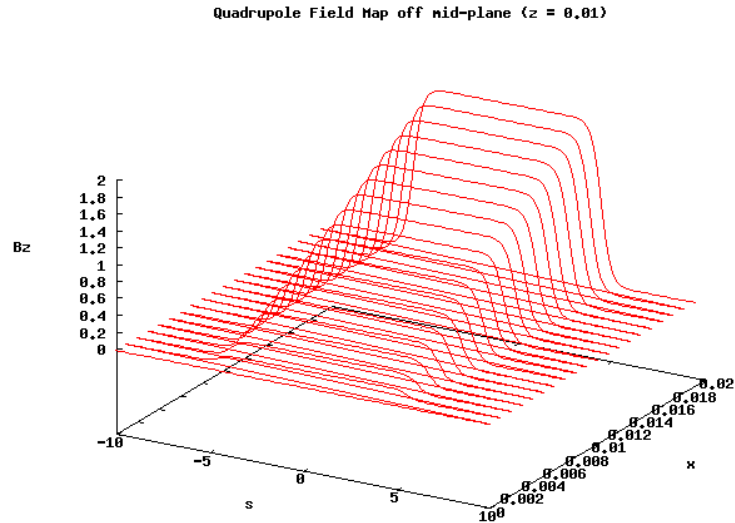


Figure 1.26: QuadrupoleT field off the mid-plane

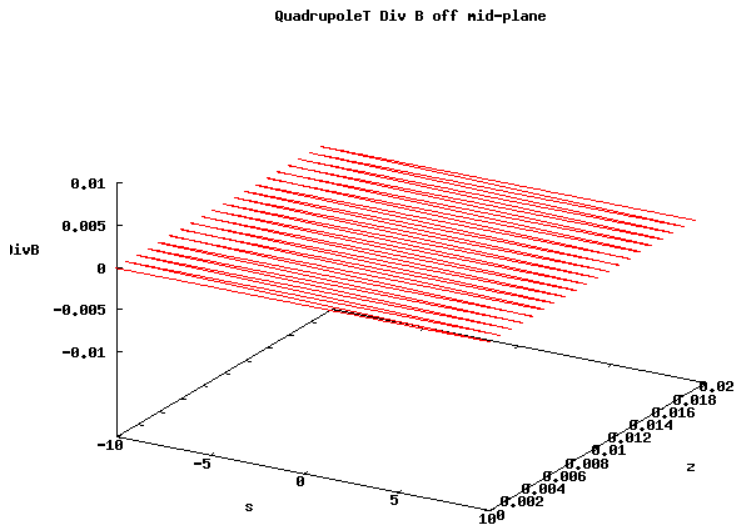


Figure 1.27:  $|\nabla \cdot \mathbf{B}|$  off the mid-plane

this case the field inside the aperture is more probable to diverge for smaller dimensions of the aperture. Thus, when setting the length of the end fields, one must make sure that the aperture is small enough for the field expansion to converge everywhere. Figures 1.29, 1.30 and 1.31 shows the behaviour of the field when going off the mid-plane for different fringe field lengths.

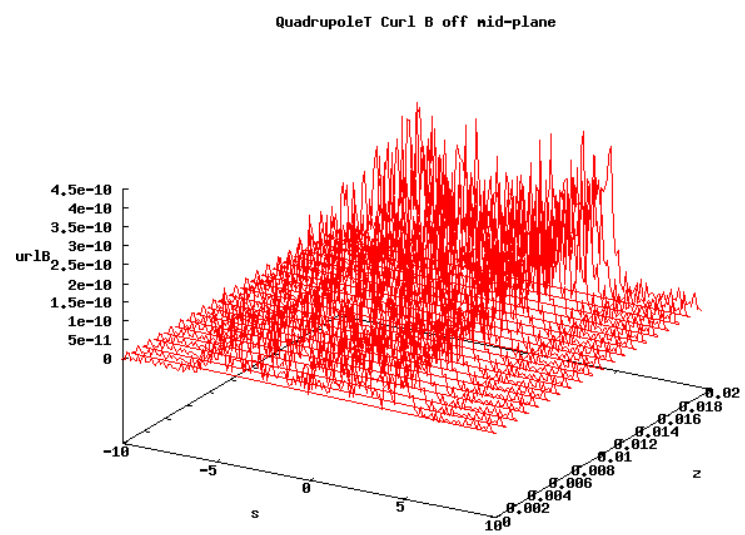


Figure 1.28:  $|\nabla \times \mathbf{B}|$  off the mid-plane

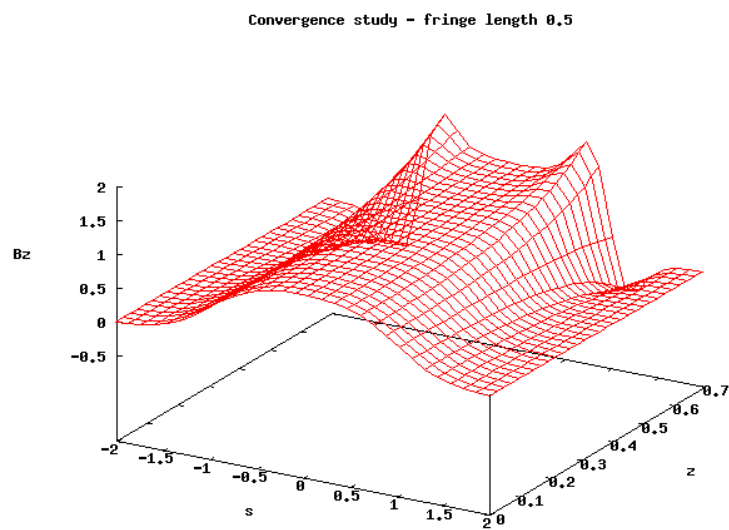


Figure 1.29: Field divergence regions

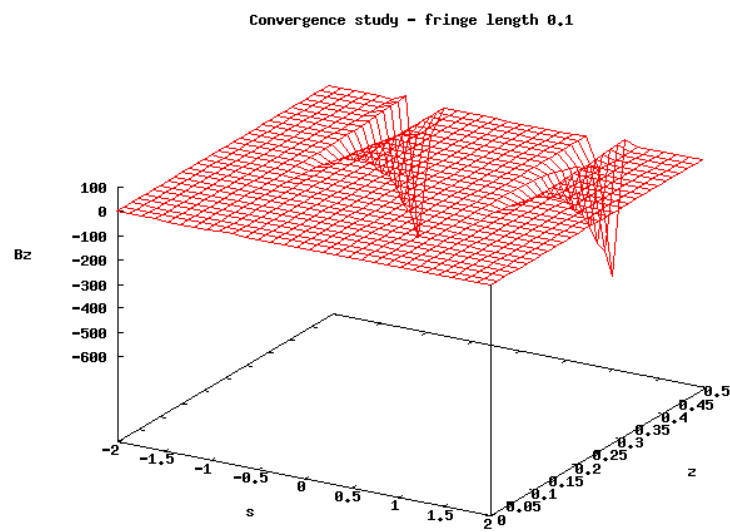


Figure 1.30: Field divergence regions

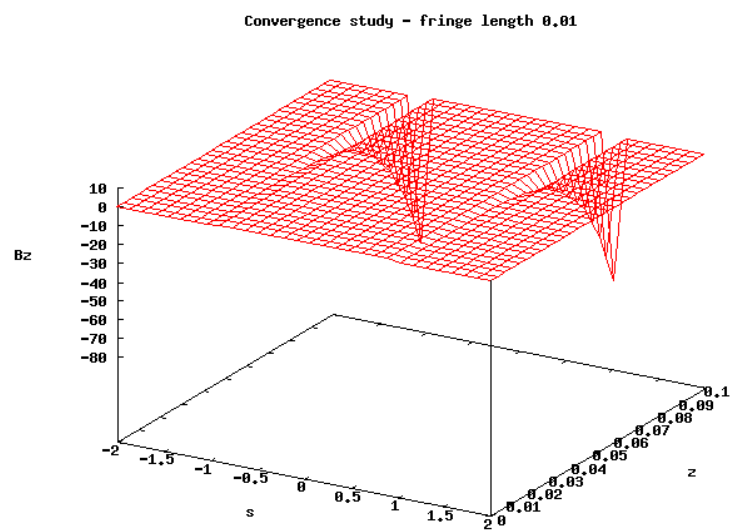


Figure 1.31: Field divergence regions

# Weeks 6-8

## 1.1 Extending the new multipole model in OPAL

The previous implementation of the MultipoleT element in OPAL was extended to include more features such as: variable radius of curvature, asymmetric fringe fields, rotation for skew fields, entrance angle. The full documentation as introduced in that of OPAL can be found below.

Some figures showing the field for a dipole and a combined function magnet (10 T dipole + 100 T/m field gradient quadrupole) generated by this model can be seen in Appendix A (the field corresponds to the variable radius expansion).

### Documentation for MultipoleT

A MULTIPOLET is in OPAL-T a general multipole with extended features. It can represent a straight or curved magnet. In the curved case, the user may choose between constant or variable radius. This model includes fringe fields.

---

label: MULTIPOLET, L=real, ANGLE=real, VAPERT=real,  
HAPERT=real, LFRINGE=real, RFRINGE=real, TP=real-vector,  
VARRADIUS=bool;

---

L Physical length of the magnet (meters), without end fields. (Default: 1 m)

ANGLE Physical angle of the magnet (radians). If not specified, the magnet is considered to be straight (ANGLE=0.0). This is not the total bending

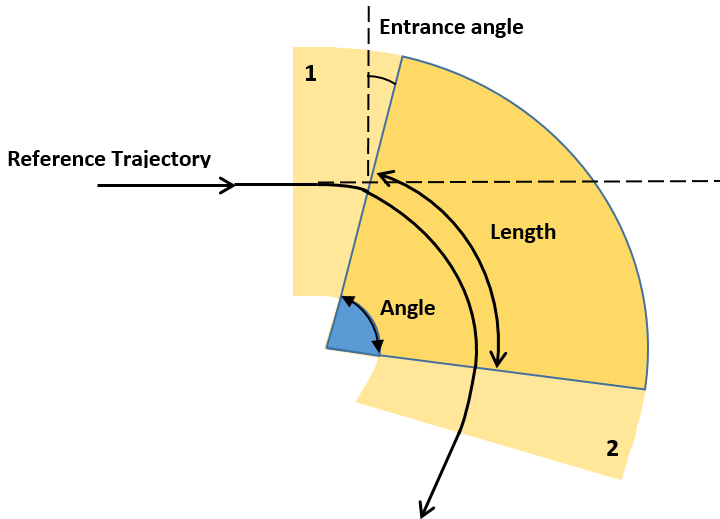


Figure 1.32: MultipoleT illustration (regions 1 and 2 represent the end fields)

angle since the end fields cause additional bending. The radius of the multipole is set from the LENGTH and ANGLE attributes.

VAPERT Vertical (non-bend plane) aperture of the magnet (meters). (Default: 0.5 m)

HAPERT Horizontal (bend plane) aperture of the magnet (meters). (Default: 0.5 m)

LFRINGE Length of the left fringe field (meters). (Default: 0.0 m)

RFRINGE Length of the right fringe field (meters). (Default: 0.0 m)

TP A real vector, containing the multipole coefficients of the field expansion on the mid-plane in the body of the magnet: the transverse profile  $T(x) = B_0 + B_1x + B_2x^2 + \dots$  is set by TP= $B_0, B_1, B_2$  (units:  $T \cdot m^{-n}$ ). The order of highest multipole component is arbitrary, but all components up to the maximum must be given, even if they are zero.

MAXFORDER The order of the maximum function  $f_n$  used in the field expansion (default: 5). See the scalar magnetic potential below. This sets for example the maximum power of  $z$  in the field expansion of vertical component  $B_z$  to  $2 \cdot \text{MAXFORDER}$ .

EANGLE Entrance edge angle (radians).

ROTATION Rotation of the magnet about its central axis (radians, counterclockwise). This enables to obtain skew fields. (Default 0.0 rad)

**VARRADIUS** This is to be set TRUE if the magnet has variable radius. More precisely, at each point along the magnet, its radius is computed such that the reference trajectory always remains in the centre of the magnet. In the body of the magnet the radius is set from the LENGTH and ANGLE attributes. It is then continuously changed to be proportional to the dipole field on the reference trajectory while entering the end fields. This attribute is only to be set TRUE for a non-zero dipole component. For a visualization see the next section. (Default: FALSE)

**VARSTEP** The step size used in calculating the reference trajectory for VARRADIUS = TRUE (meters). It specifies how often the radius of curvature is re-calculated. This has a considerable effect on tracking time. (Default: 0.1 m)

Superposition of many multipole components is permitted. The reference system for a multipole is a Cartesian coordinate system for straight geometry and a  $(x, s, z)$  Frenet-Serret coordinate system for curved geometry. In the latter case, the axis  $\hat{s}$  is the central axis of the magnet.

The following example shows a combined function magnet with a dipole component of 2 Tesla and a quadrupole gradient of 0.1 Tesla/m.

M30: MULTIPOLET, L=1, RFRINGE=0.3, LFRINGE=0.2,  
ANGLE=PI/6, TP={2.0, 0.1}, VARRADIUS=TRUE;

The field expansion used in this model is based on the following scalar potential:

$$V = zf_0(x, s) + \frac{z^3}{3!}f_1(x, s) + \frac{z^5}{5!}f_2(x, s) + \dots \quad (138)$$

Mid-plane symmetry is assumed and the vertical component of the field on the mid-plane is given by the user under the form of the transverse profile  $T(x)$ . The full expression for the vertical component is then

$$B_z = f_0 = T(x) \cdot S(s) \quad (139)$$

where  $S(s)$  is the fringe field. This element uses the Tanh model for the end fields, having only three parameters (the centre length  $s_0$  and the fringe field lengths  $\lambda_{left}$ ,  $\lambda_{right}$ ):

$$S(s) = \frac{1}{2} \left[ \tanh\left(\frac{s + s_0}{\lambda_{left}}\right) - \tanh\left(\frac{s - s_0}{\lambda_{right}}\right) \right] \quad (140)$$

Starting from Maxwell's laws, the functions  $f_n$  are computed recursively and finally each component of the magnetic field is obtained from  $V$  using the corresponding geometries.

## 1.2 VARRADIUS attribute

This section provides a couple of figures to better understand how the VARRADIUS attribute modifies the geometry of the MultipoleT OPAL element. The figures (1.33) and (1.34) are intended to show the difference between the shape of the field when the VARRADIUS attribute is set to FALSE and TRUE, respectively. The orientation, dimensions and field strength of these two magnets are the same. As it can be observed, in the figure (1.33) the end fields have the same curvature as the body of the magnet, while in figure (1.34) the curvature of the end fields approaches zero as does the field

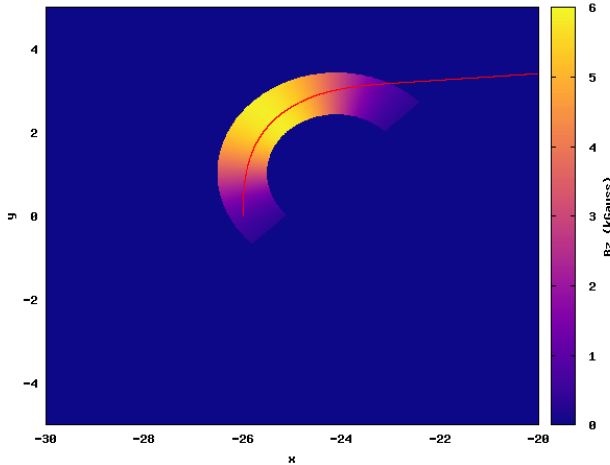


Figure 1.33: Constant radius dipole + particle trajectory

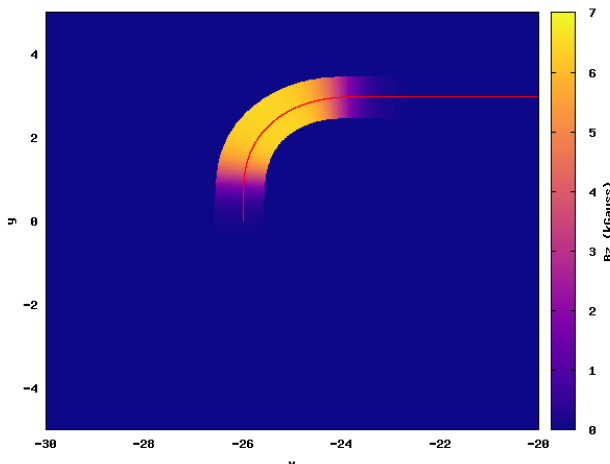


Figure 1.34: Variable radius dipole + particle trajectory

### 1.3 Tracking ISIS with OPAL

The previously described element was used to model the dipoles and quadrupoles existing in the ISIS synchrotron ring. We have built the 10-fold symmetric lattice from an older description which used small dipoles/quadrupoles to model the end fields. However, in our lattice there was no need for this magnets since the end fields are taken care of by the new OPAL element. Therefore, the old lattice file represented only a starting point from which small adjustments were made to the length, fringe lengths or bending angle of the magnets until we were able to contain the beam inside the accelerator.

Figure (1.35) shows the trajectory of the particle inside the accelerator for 100 turns. The focusing/defocusing effects of the quadrupoles (and even of the dipoles) are considerably visible. Figure (1.36) shows a phase-space diagram for 2 turns and the ellipse fit.

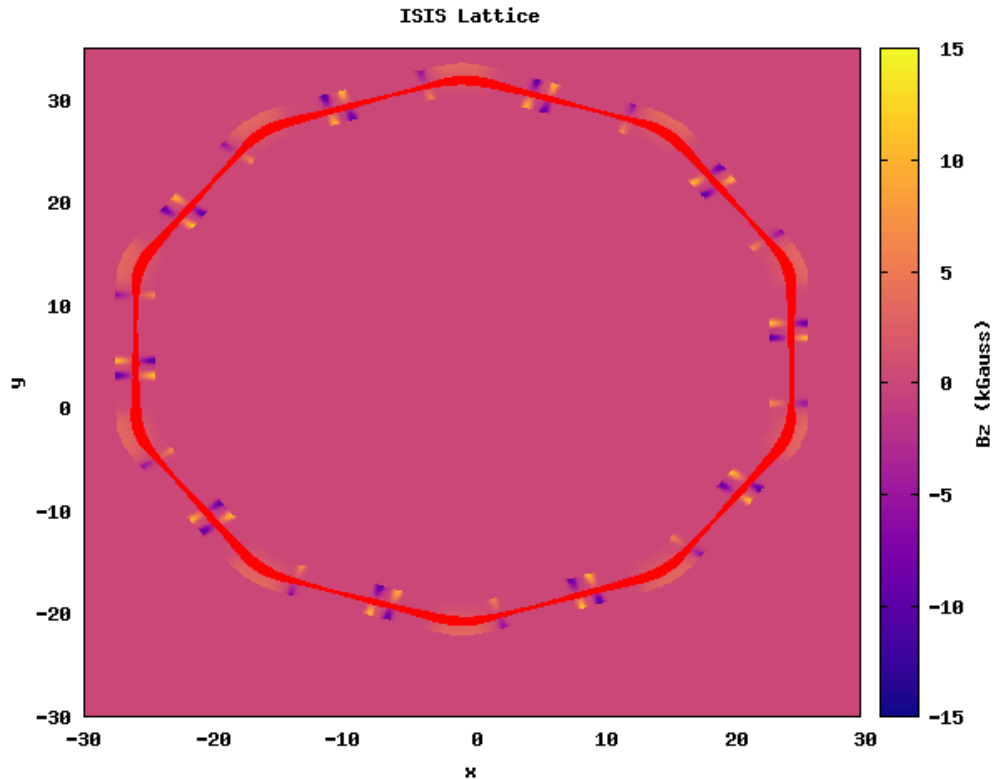


Figure 1.35: Tracking one particle for 100 turns (trajectory in red)

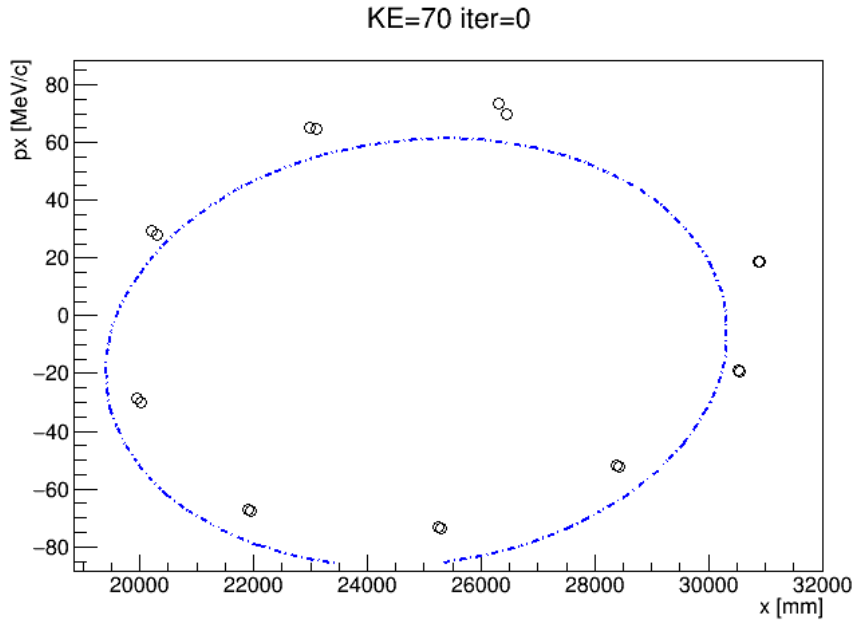


Figure 1.36: Phase space diagram (near closed orbit) + ellipse fit

### 1.3.1 Tracking CPU time

In order to obtain an approximation of the time required to track many particles (e.g.  $10^6$ ) for an arbitrary number of turns around the ISIS accelerator we make a note of the CPU time required in tracking one particle.

When using the constant radius element for the ISIS dipoles, the total CPU time was 2,628 for one particle and 100 turns. From this total time, an amount of 2,411 was spent for the integration of the particle's motion.

By contrast, the total CPU time was 503 for a particle and 1 turn when using the variable radius model for the ISIS dipoles. Assuming a linear relationship, this implies an approximate CPU time of 50,000 for 100 turns which is by a factor of 20 higher than that required when using the simpler model. This is expected since additional tracking needs to be done to determine the geometry of magnet in this case. We can reduce the tracking time by setting a lower value for the VARSTEP attribute, but this also reduces the precision with which the shape of the magnet is determined, making the field less smooth. Decreasing the VARSTEP value by a factor of 4 increases the CPU total time from 503 to 1892 for 1 turn. Therefore, we may consider a linear relation between these two variables.

A possible solution to decrease the total CPU time and still use the more

complex model is to use OPAL to generate the field map for the accelerator. Afterwards, the field map may be used by OPAL or another tracking code, thus avoiding the repeated computation of the shape of the magnets while tracking.

# References

- [1] J. Rossbach, P. Schmusser. *Basic course on accelerator optics*. CERN Accelerator School, pp.17-88 (CERN-1994-001), 1993.  
<http://dx.doi.org/10.5170/CERN-1994-001.17>
- [2] S. Caspi, M. Helm, L.J. Laslett *3D Field Harmonics*. Lawrence Berkeley Laboratory, University of California Berkeley, CA 94720, March 1991.
- [3] S. Y. Lee. *Accelerator Physics*. Indiana University, World Scientific Publishing, 1999, pp. 20-40.
- [4] G.I. Bell, D.T. Abell. *Fringe field simulations of a non-scaling FFAG accelerator*. Texh-X Corporation, Boulder CO 80303, February 2012, arXiv:1202.0805.

## Appendix A

### Field maps

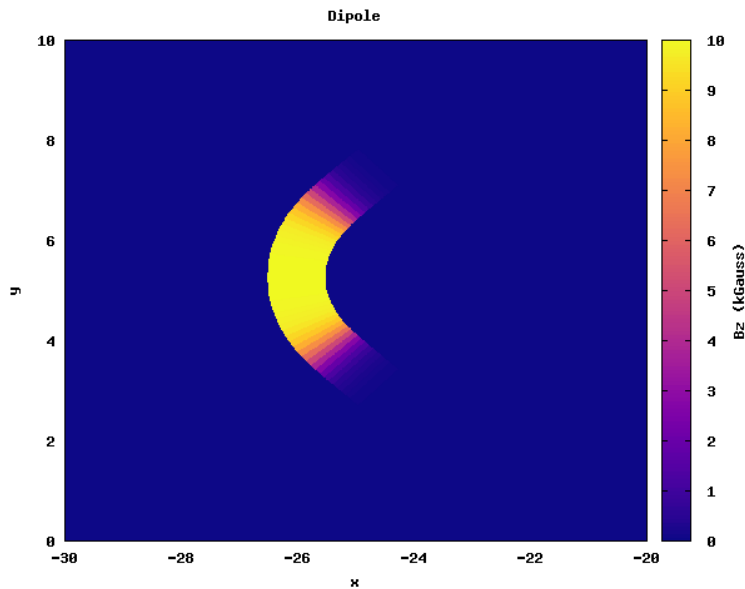


Figure 1.37: Dipole field component  $B_z$  (variable radius)

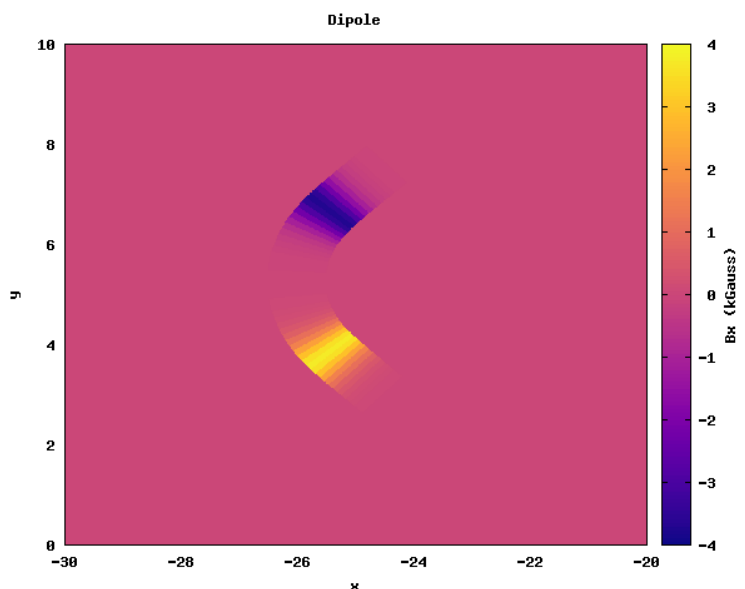


Figure 1.38: Dipole field component  $B_x$  (variable radius)

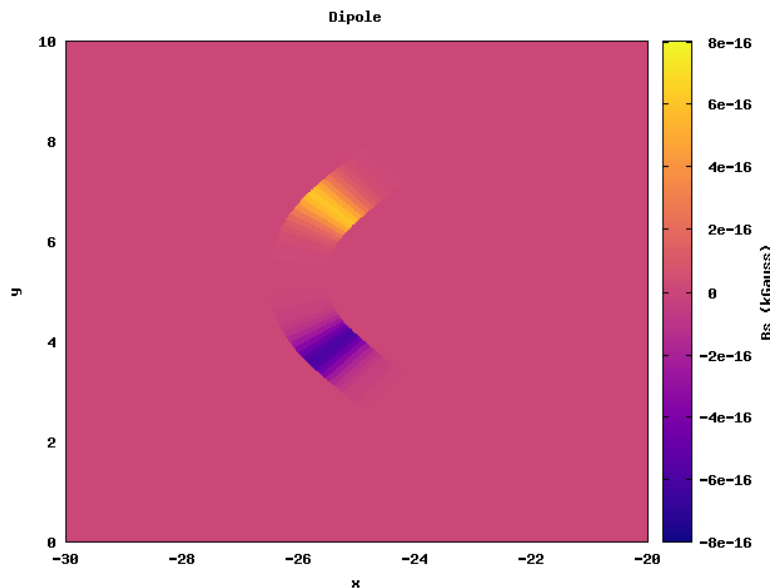


Figure 1.39: Dipole field component Bs (variable radius)

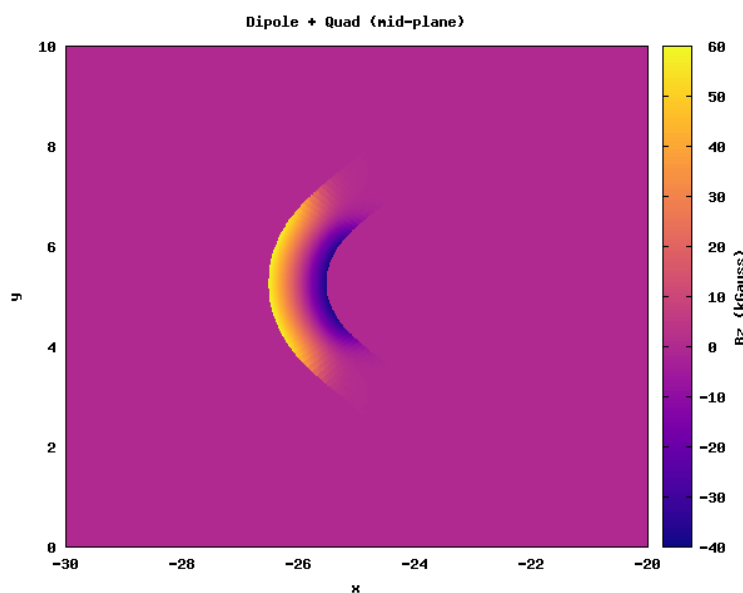


Figure 1.40: Combined function multipole(variable radius) - field component Bz ( $B_x, B_s = 0$ ) - mid-plane

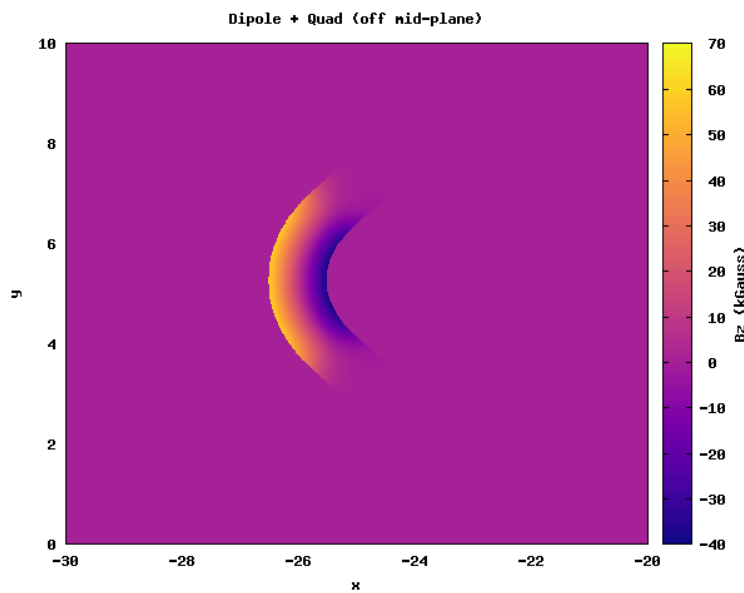


Figure 1.41: Combined function multipole(variable radius) - field component Bz - off mid-plane

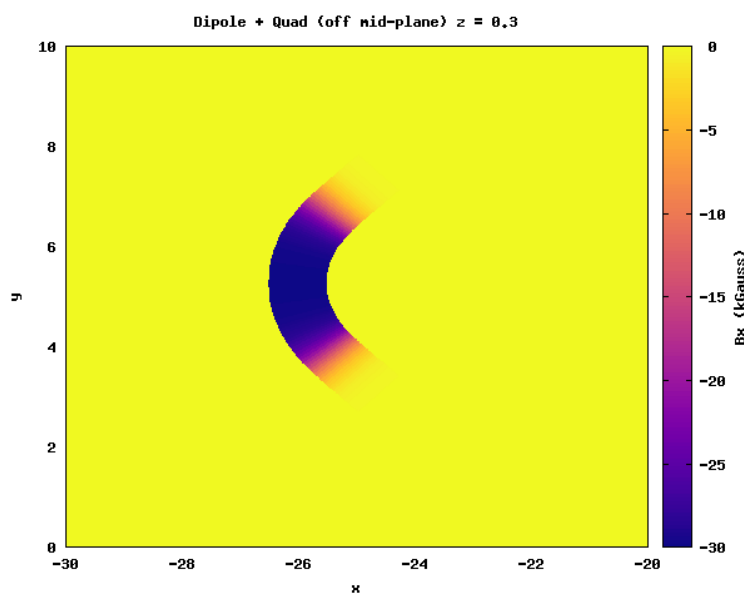


Figure 1.42: Combined function multipole(variable radius) - field component Bx - off mid-plane

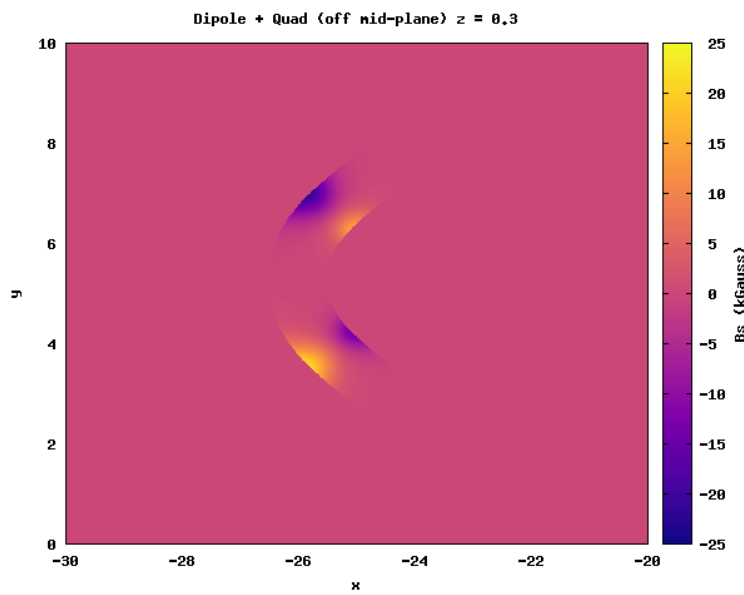


Figure 1.43: Combined function multipole(variable radius) - field component  
Bs - off mid-plane

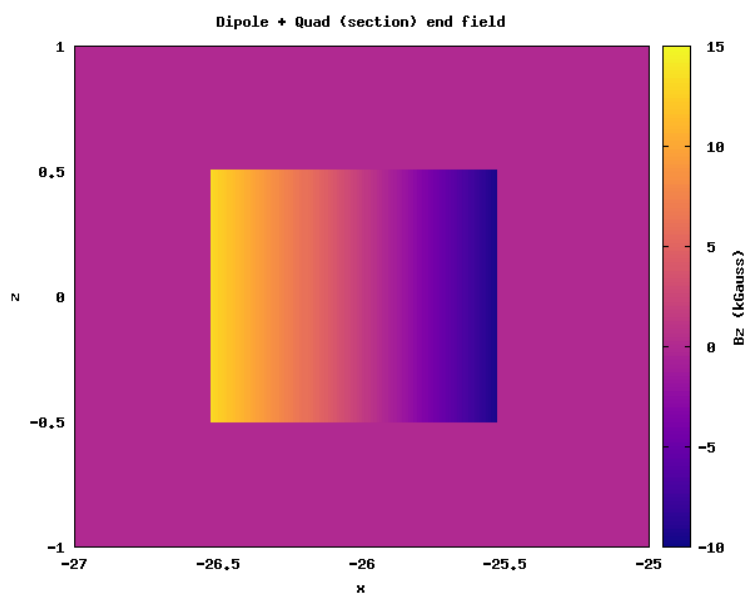


Figure 1.44: Combined function multipole(variable radius) - field component  
Bz - section in end field

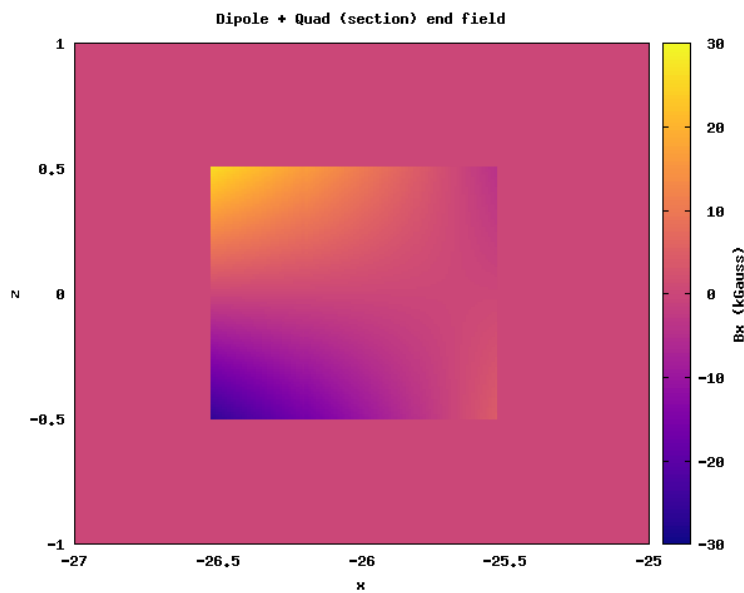


Figure 1.45: Combined function multipole(variable radius) - field component  $B_x$  - section in end field

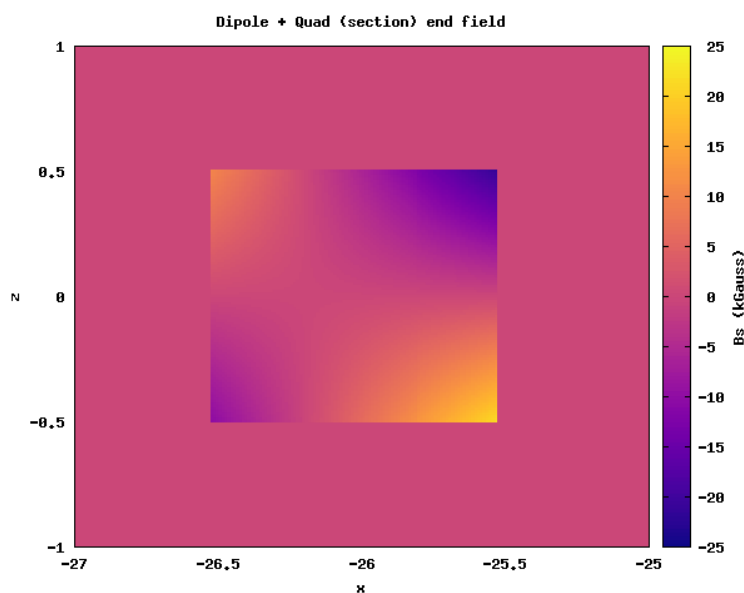


Figure 1.46: Combined function multipole(variable radius) - field component  $B_s$  - section in end field